

# DIFFUSION BRIDGES FOR STOCHASTIC HAMILTONIAN SYSTEMS WITH APPLICATIONS TO SHAPE ANALYSIS

ALEXIS ARNAUDON, FRANK VAN DER MEULEN, MORITZ SCHAUER,  
AND STEFAN SOMMER

ABSTRACT. Stochastically evolving geometric systems are studied in geometric mechanics for modelling turbulence parts of multi-scale fluid flows and in shape analysis for stochastic evolutions of shapes of e.g. human organs. Recently introduced models involve stochastic differential equations that govern the dynamics of a diffusion process  $X$ . In applications  $X$  is only partially observed at times 0 and  $T > 0$ . Conditional on these observations, interest lies in inferring parameters in the dynamics of the diffusion and reconstructing the path  $(X_t, t \in [0, T])$ . The latter problem is known as bridge simulation. We develop a general scheme for bridge sampling in the case of finite dimensional systems of shape landmarks and singular solutions in fluid dynamics. This scheme allows for subsequent statistical inference of properties of the fluid flow or the evolution of observed shapes. It covers stochastic landmark models for which no suitable simulation method has been proposed in the literature, that removes restrictions of earlier approaches, improves the handling of the nonlinearity of the configuration space leading to more effective sampling schemes and allows to generalise the common inexact matching scheme to the stochastic setting.

## 1. INTRODUCTION

**1.1. Background.** The geometry of landmark spaces and the landmark matching problem, exemplified by matching of finite sets of anatomical markers on medical images, has been extensively studied in shape analysis. References include the seminal work of Kendall [22] on landmark configurations modulo scaling and rotation, and the extensive interest of landmark dynamics for diffeomorphic shape models [21, 43]. The landmark matching problem has a geometric formulation in the language of geometric mechanics where diffeomorphisms of the underlying domain act to move the landmarks, and optimal trajectories between observed landmark configurations satisfy geodesic equations for a right-invariant metric on the diffeomorphism group [44]. These equations are also called Euler-Poincaré equations [18]. Landmark dynamics are intrinsically linked to soliton dynamics in fluid dynamics [19], e.g. soliton solutions of the Camassa-Holm equations [11], or more generally singular solutions of the Euler-Poincaré equation [16]. Stochastic models of landmark evolutions are therefore of interest in both shape analysis and fluid dynamics.

Several recent models include stochastic effects in landmark analysis [26, 39, 42, 27, 1, 2]. The interest here appears for several reasons:

---

*Date:* June 12, 2025.

*Key words and phrases.* Shape analysis, conditional diffusion, hypoelliptic diffusion, bridge simulation, landmark dynamics, guided proposals, shape matching.

- (1) If  $v$  denotes the observed landmark configuration, the presence of noise in the observation implies that landmark analysis is classically performed in the inexact setting where the requirement that the flow  $q_t$  satisfy  $q_T = v$  at observation time  $t = T$  is essentially relaxed to  $q_T = v + \epsilon$  for some perturbation  $\epsilon$ . This thus amounts to adding noise at the endpoint  $q_T$  of the flow  $q_t$ . If the perturbation is not linked to observation noise but instead comes from intrinsic stochastic behaviour of the shape or soliton evolution, it is more natural to make the noise intrinsic time-continuous, i.e. added to  $q_t$  for each  $t$  on an infinitesimal level.
- (2) The flow  $q_t$  can have multi-scale behaviour where the coarse scale evolution is modeled by a deterministic flow while the fine scale behaviour, which in a fluid system is closer to turbulence, can be summarised with stochastic terms.
- (3) In medical applications, it can be hypothesised that a component of the shape evolution arise from non-deterministic events such as cell growth or death, and that these happen continuously in time.
- (4) It is generally hard to construct natural families of probability distributions on geometric spaces without linearising the spaces around a center point. Solutions to stochastic differential equations however provide such probability models.

In this paper, we focus on models defined by stochastic differential equations. In all of the above enumerated cases, it is common that observations are discrete in time and only part of the state space of the process is observed. Constructing paths that are conditioned on such partial observations is called *bridge simulation* and the paths *bridges*. Bridge simulation is essential for likelihood based inference as it provides a stochastic method for approximating the intractable likelihood. If possible, it enables methods such as sequential Monte Carlo, Markov Chain Monte Carlo, stochastic Expectation-Maximisation, or stochastic gradient descent. This in turn allows for estimation of parameters in the process' dynamics and recovery of latent states at observation times. Moreover, in applications like landmark matching, there is intrinsic interest in bridge simulation as bridges appear as stochastic perturbations of landmark geodesics or as critical paths for a stochastically perturbed energy. Bridges therefore present a stochastic generalisation of the geodesic paths usually considered when matching sets of landmarks. Bridge simulation is generally a challenging problem. It has been addressed in the Euclidean setting in a series of works including [12, 7, 31, 9, 36].

For shape manifolds, previous papers have centred on simulation in landmark spaces. Manifolds of finite numbers of landmarks are generally of finite dimensionality in contrast to spaces of continuous shapes which are in essence infinite dimensional. While bridge sampling on infinite dimensional shape spaces remains an open question, bridge sampling for landmarks spaces has been considered recently [1, 2, 37] using the approach of [12, 25]. The underlying diffusion arises from stochastic Euler-Poincaré equations [15] and, in a different setting, Brownian motion on the landmark space [37]. The difficulty in landmark bridge sampling arises from the high-dimensionality, the curvature and hence nonlinearity of the diffusion process, the degenerate diffusion processes in the stochastic Euler-Poincaré case (vanishing eigenvalues in the diffusion matrix), and from observations being only in the position variable of the phase-space flow. The methods from [12] and [1, 2] apply only for certain classes of stochastic evolution, excluding other important stochastic landmark approaches such as proposed in [39, 27], due to the degeneracy of the flow. As stated in [27] “Unfortunately, none of the known methods for diffusion bridges

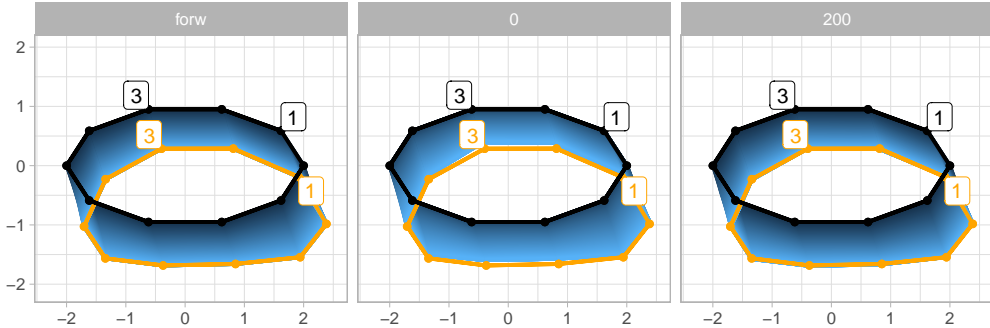


FIGURE 1. Simulations with the TV-model (parameters  $c = \gamma = 0.2$ ,  $a = 0.49$ ), details are in Section 6). The left figure shows forward simulated landmarks shapes (i.e. polygons that connect landmark bridges at fixed times) where all landmarks have initial momentum  $(1, -3)$ . The middle figure shows the evolution of shapes at the initialisation of our algorithm when all initial momenta are set to zero. The right figure shows the evolution after 200 iterations where both bridges and momenta have been updated. Notice that even when the initial landmarks are initialised incorrectly (middle figure), the resulting shapes are visually hard to distinguish from the forward simulated bridges. The left- and right figure are visually indistinguishable. Figure 2 confirms that the initial momenta of the bridges are estimated correctly at iteration 200. The two labeled landmarks correspond to the facets in that figure.

works with (2.1) to give computationally convenient algorithms. Without an efficient method for sampling the diffusion bridge, it is hard to formulate an MCMC method with good acceptance rates. Consequently, the generalised Langevin prior distribution is difficult to use in Bayesian statistics, and we now turn to simpler prior distributions, which arise by approximating the Langevin equation.” Equation (2.1) in [27] is equation (10) in the present paper, and, using the presented methods, we show that resorting to such simpler prior distributions is unnecessary. In Figures 1 and 2 we demonstrate that our method yields satisfactory bridges with accurate recovery of initial momenta.

**1.2. Contribution.** We extend the Euclidean simulation approach of [36, 8] to a general method for simulating stochastic landmark equations. We will pursue this under two different stochastic models for landmark and soliton dynamics (those introduced in [39] and [1]). The presented method is the first in the literature to allow bridge sampling for the former scheme, and it improves upon previous sampling schemes by better incorporating nonlinearity in the drift and diffusion coefficients of the SDEs. For models with intrinsic noise it is the first approach that provides full uncertainty quantification via

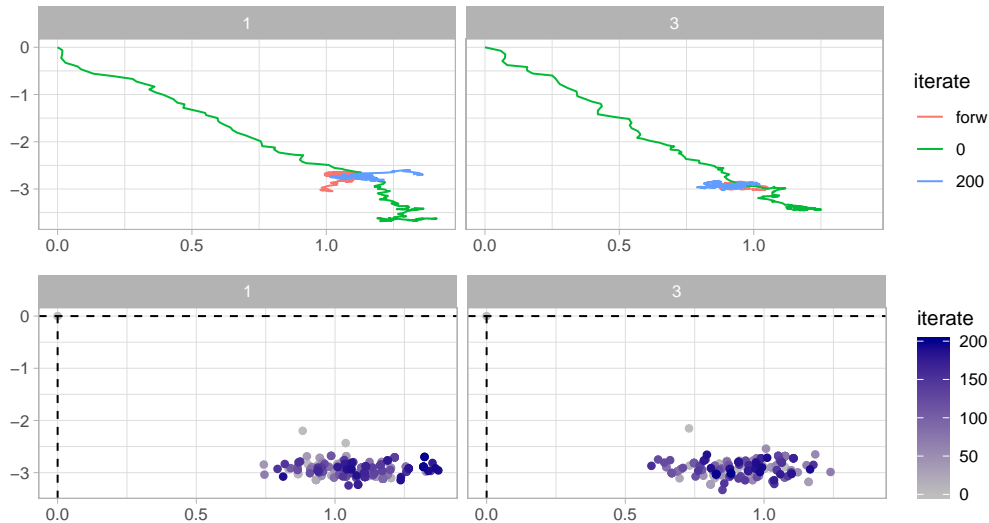


FIGURE 2. Same setting as in Figure 1. The panels refer to landmarks indexed by 1 (left) and 3 (right). The top panel shows trajectories for the momenta for the forward simulated path, as also for the bridges at initialisation and iteration 200. The bottom panel shows iterates of the initial momentum, the data-generating momentum being  $(1, -3)$  for all landmarks. Note that the initial momenta at iteration 0 are completely wrong (corresponding to the begin of the green curve in top panel), but the algorithm reaches its stationary regime within 10 iterates.

samples of the posterior. Additional novel features are generalising the notion of inexact shape matching as in [43] and using the Riemannian Manifold Metropolis Adjusted Langevin Algorithm (RMMALA) for efficient updates in template estimation.

**1.3. Outline.** The paper starts in Section 2 with a review of finite dimensional shape analysis and its stochastic extensions. In Section 3 we explain how guided proposals can be used for bridge simulation. Their specific implementation for the two stochastic landmarks models considered in this work is specified in Section 4. Markov Chain Monte Carlo sampling schemes are detailed in Section 5 and experimental evaluation on synthetic and empirical datasets are given in Section 6. We end with a discussion section with suggestions for future work.

## 2. FINITE DIMENSIONAL SHAPE ANALYSIS

To provide the necessary background for the stochastic landmark models, we here give a short review of landmark shape spaces with geometry inherited from a right-invariant metric on the diffeomorphism group. Landmark shape spaces are finite dimensional in contrast to spaces of continuous curves and surfaces that are inherently infinite dimensional. On a formal level, the geometric setting as outlined below is however equivalent. This makes the landmark case an example of how stochastics and bridge simulation can

be used in a geometric setting while we can postpone the intricacies of infinite dimensionality in other shape spaces to later works.

Shape analysis as pursued in the Large Deformation Diffeomorphic Metric Mapping (LDDMM, [43]) framework starts with actions of the diffeomorphism group on shapes spaces. For landmarks, let  $q = (q_1, \dots, q_n)$  be a configuration of  $n$  distinct landmarks  $q_i \in \Omega$  in a domain  $\Omega \subset \mathbb{R}^d$ . Let  $\varphi$  be an element of the set  $\text{Diff}(\Omega)$  of diffeomorphism on  $\Omega$ , smooth invertible mappings with smooth inverses. Then  $\varphi$  acts on  $q$  by composition  $\varphi.q = (\varphi(q_1), \dots, \varphi(q_n))$ . For fixed  $q$ , the map  $\pi: \text{Diff}(\Omega) \rightarrow \mathcal{M}$ ,  $\pi(\varphi) = \varphi.q$  is denoted the action map.

The landmark space  $\mathcal{M} = \{(q_1, \dots, q_n) \in \Omega^n \mid q_i \neq q_j, i \neq j\}$  can be given the structure of a manifold by letting it inherit the differentiable structure from its embedding as an open subset of  $\mathbb{R}^{nd}$  ( $\mathbb{R}^{nd}$  except for the subset of points where landmark pairs coincide). It can furthermore be equipped with a Riemannian metric which in turn defines the length and energy of path in the landmark space, and from this the matching energy (4) used below is defined. This happens with the following geometric structure.

**1)** Let  $\mathcal{X}(\Omega)$  be the space of vector fields on  $\Omega$ . We equip subsets  $V$  of  $\mathcal{X}(\Omega)$  with an inner product using a reproducing kernel Hilbert space (RKHS) structure: For  $q_1, \dots, q_n \in \Omega$  let  $V$  be the completion of the set of vector fields on the form  $\sum_{i=1}^n K(\cdot, q_i)a_i$ ,  $a_i \in \mathbb{R}^d$ . Here  $K: \Omega \times \Omega \rightarrow \mathbb{R}^{d \times d}$  is a matrix-valued map denoted a kernel.  $K$  is required to be symmetric and positive definite in the sense that

$$\sum_{i,j=1}^n a_i^T K(q_i, q_j) b_j > 0 \quad \forall a_i, b_j \in \mathbb{R}^d, q_i, q_j \in \Omega, n \in \mathbb{N}.$$

In this case,  $V$  receives an inner product by completing the inner product

$$\langle K(\cdot, q_i)a_i, K(\cdot, q_j)b_j \rangle_V = \sum_{i,j=1}^n a_i^T K(q_i, q_j) b_j, \quad (1)$$

to all of  $V$  by continuity. This makes  $V$  a Hilbert space.

**2)** Since  $\mathcal{M} \subset \mathbb{R}^{nd}$ , tangent vectors  $v \in T\mathcal{M}$  can be represented as vectors in  $\mathbb{R}^{nd}$ . Let  $q \in \mathcal{M}$  be a landmark configuration. The LDDMM Riemannian metric is then the inner product

$$\langle v, w \rangle_q = \sum_{i,j=1}^n v_i^T K(q_i, q_j)^{-1} w_j \quad (2)$$

between vectors  $v, w \in T_q\mathcal{M}$ . Landmark dynamics are often described in terms of momenta, covectors in the dual bundle  $T^*\mathcal{M}$ . The corresponding inner product between momentum vectors  $a, b \in T_q^*\mathcal{M}$  (the cometric) is then

$$\langle a, b \rangle_q = \sum_{i,j=1}^n a_i^T K(q_i, q_j) b_j, \quad (3)$$

i.e., the cometric coincides with the inner product (1) on  $V$ .

**3)** The Riemannian structure on  $\mathcal{M}$  described here has its geometric origin in the following facts: The tangent space  $T_{\text{Id}} \text{Diff}(\Omega)$  of the Lie group  $\text{Diff}(\Omega)$  is diffeomorphic to  $\mathcal{X}(\Omega)$ , and the Riemannian metric (2) is the Riemannian metric on  $\mathcal{M}$  that makes the action map  $\pi$  above a Riemannian submersion with respect to the right-invariant

(invariant to the composition of diffeomorphisms on the right) Riemannian metric on  $\text{Diff}(\Omega)$  that the inner product (1) on  $V \subset \mathcal{X}(\Omega)$  specifies. In the current context, the main implication of this geometric argument is that the metric (2) and cometric (3) have their definitions rooted on a well-defined geometric structure.

The Riemannian metric defines the energy of a path  $\mathbf{q} = (q_t, t \in [0, T])$  of landmark configurations by

$$E(\mathbf{q}) = \int_0^T \langle \dot{q}_s, \dot{q}_s \rangle_q ds.$$

This allows matching of landmark configurations  $q$  and  $v$  by searching for a minimal energy path  $\mathbf{q}$ ,  $q_t \in \mathcal{M}$  such that  $q_0 = q$  and  $q_T = v$ ,

$$\underset{\mathbf{q}, q_0=q, q_T=v}{\text{argmin}} E(\mathbf{q}), \quad (4)$$

as pursued below. Paths realising this energy are geodesics on  $\mathcal{M}$ .

**2.1. Inverse problem of landmark matching.** The interest in landmark matching arises from the case where a fixed sets of meaningful landmarks, for example anatomical markers in medical images, can be identified. Shapes can then be analysed by identifying differences between configurations of markers, in the medical case either between subjects or intra-subject when consecutive images are acquired over time. Interestingly, the LDDMM framework allows matching of landmarks as well as curves, surfaces and even images on  $\Omega$  via the same framework with a metric on  $\text{Diff}(\Omega)$  descending to the particular shape spaces. However, we will restrict to the landmark case here for two primary reasons: The landmark manifold  $\mathcal{M}$  is finite dimensional, and it has a natural embedding in  $\mathbb{R}^{nd}$  allowing us to write landmark dynamics in Euclidean coordinates.

Assume two landmark configurations  $q$  and  $v$  are given. A matching consists in solving the variational problem

$$\underset{\mathbf{q}}{\text{argmin}} E(\mathbf{q}) \quad \text{such that} \quad q_0 = q, q_1 = v, \quad (5)$$

with the energy  $E$  from (4). This is known as exact matching and results in a  $t$ -dependent transformation of the configuration  $q$  to the configuration  $v$ . Due to the uncertainty often present in observations of landmarks, e.g. with manual annotations on medical images, inexact matching is instead often used in practice. The variational problem is now

$$\underset{\mathbf{q}}{\text{argmin}} E(\mathbf{q}) + S(q_1, v) \quad \text{such that} \quad q_0 = q, \quad (6)$$

with the added term  $S$  measuring the dissimilarity between the two landmark configurations  $q_1$  and  $v$ . This term is often taken to be of the form  $S(q_1, v) = n^{-1} \|q_1 - v\|^2$  using the norm from the embedding of  $\mathcal{M}$  in  $\mathbb{R}^{nd}$ . Intuitively, we can think of Gaussian noise on the observations in  $\mathbb{R}^{nd}$  and  $S$  being proportional to a log-likelihood.

Note that the  $t$ -dependence of solutions to (5) and (6) allows us to think of  $q_1$  as an observation of landmark trajectories  $q_t$  at time  $t = 1$ . This will in particular relate to the conditioning of stochastic processes later, where we assume a fixed observation time  $T > 0$ . In the matching case, the notation implies  $T = 1$  without loss of generality.

**2.2. Deterministic landmark dynamics.** The energy (4) has a Hamiltonian formulation which involves the kernel  $K$ , where the Hamiltonian is

$$H(q, p) = \frac{1}{2} \langle p, p \rangle_q = \frac{1}{2} \sum_{i,j=1}^n p_i^T K(q_i, q_j) p_j. \quad (7)$$

Let  $x \in \mathbb{R}^{2dn}$  be the vector obtained by concatenating the tuples  $\{(q_i, p_i)\}_{i=1}^n$ . That is,  $x$  represents an element of the phase space  $T^*\mathcal{M}$  of the landmark space. Let  $K$  be a kernel as discussed above, and we assume it is scalar, i.e. of the form  $K(y) = k(y) \text{Id}_d$  for a real-valued function  $k$ . Hamilton's equations of motion are then explicitly given by

$$\begin{aligned} \frac{d}{dt} q_i &= \sum_{j=1}^n p_j k(q_i - q_j), \\ \frac{d}{dt} p_i &= - \sum_{j=1}^n \langle p_i, p_j \rangle \nabla k(q_i - q_j), \end{aligned} \quad (8)$$

where  $p$  is the momentum of the flow and  $\nabla k(y)$  the gradient of  $k$ .

Solutions  $\mathbf{q}$  to (5) and (6) appear as the  $q$ -variable of solutions  $(\mathbf{q}, \mathbf{p})$  to (8). Therefore, the search space for optimal solutions of the optimization problems can be reduced to solutions of Hamilton's equations, a reduction from an infinite to a finite dimensional space.

**2.3. Stochastic landmark dynamics.** As already indicated, there are several reasons to introduce stochastic evolutions. We review here two different models of stochastic evolutions on landmarks which we will consider later.

**2.3.1. Stochastic forcing: TV- and MS-model.** The first stochastic perturbation of the dynamics landmarks described above has been introduced in [39, 42] and consist in an additive Lagrangian noise of the form

$$dq_i^\alpha = \frac{\partial H}{\partial p_i^\alpha} dt \quad \text{and} \quad dp_i^\alpha = - \frac{\partial H}{\partial q_i^\alpha} dt + \gamma_i dW_t^i, \quad (9)$$

where  $\gamma_i \in \mathbb{R}$  is a scalar noise amplitude given for each landmark. We will refer to this system as the *TV-model*.

More recently, [27] generalised the TV-model by adding a dissipative term to the model:

$$dp_i^\alpha = -\lambda \frac{\partial H}{\partial p_i^\alpha} dt - \frac{\partial H}{\partial q_i^\alpha} dt + \gamma_i dW_t^i, \quad (10)$$

where  $\lambda > 0$  is a damping coefficient which enables using existence of the Gibbs invariant measure for this SDE. This model is in the following referred to as the *MS-model*.

**2.3.2. Transport noise: AHS-model.** In addition to the Lagrangian noise of the previous model (where each Wiener process is associated to a landmark), [2] introduced an Eulerian noise, where the noise fields are functions of the domain  $\Omega$ . In general, any set of functions could be used, but in practice, we will fix a family of  $J$  noise fields  $\sigma_1, \dots, \sigma_l, \dots, \sigma_J$ , which are kernel functions centred at locations  $\{\delta_\ell\}$  of the form

$$\sigma_\ell^\alpha(q) = \gamma_\alpha \bar{k}_\tau(q - \delta_\ell), \quad (11)$$

where  $\bar{k}_\tau$  is a kernel with length-scale  $\tau$  and  $\gamma \in \mathbb{R}^d$  is the vector of noise amplitudes. Note that it is possible to choose both  $\gamma$  and  $\tau$  dependent on the location  $\delta_\ell$ , though we will not use this flexibility here.

The stochastic dynamics are then obtained as in the deterministic case, to be a Hamiltonian system but in both the drift and the noise. It reads, in Stratonovich form,

$$\begin{aligned} dq_i &= \frac{\partial H}{\partial p_i} dt + \sum_{l=1}^J \sigma_l(q_i) \circ dW_t^l, \\ dp_i &= -\frac{\partial H}{\partial q_i} dt - \sum_{l=1}^J \frac{\partial}{\partial q_i} (p_i \cdot \sigma_l(q_i)) \circ dW_t^l. \end{aligned} \tag{12}$$

We will refer to this system as the *AHS-model*.

### 3. BRIDGE SIMULATION USING GUIDED PROPOSALS

All models of the previous section can be written in the general Itô form

$$dX_t = b(t, X_t) dt + \sigma(t, X_t) dW_t, \quad X_0 = x_0, \quad t \in [0, T], \tag{13}$$

where  $b: [0, T] \times \mathbb{R}^N \rightarrow \mathbb{R}^N$  and  $\sigma: [0, T] \times \mathbb{R}^N \rightarrow \mathbb{R}^{N \times N'}$  are the drift and diffusion coefficient respectively and  $W$  is a Wiener process in dimension  $\mathbb{R}^{N'}$  with independent components.

In its most basic form, the previous problems correspond to simulating trajectories of  $X := (X_t, t \in [0, T])$ , where both  $X_0$  and  $X_T$  are partially observed. We will assume that realisations of the random vectors  $V_0$  and  $V_T$  are observed, where

$$V_0 = L_0 X_0 \quad \text{and} \quad V_T = L_T X_T. \tag{14}$$

As an example, if only landmarks positions are observed at times 0 and  $T$ , then  $L_0 = L_T$  and  $L_0$  is such that  $L_0 X_t$  extracts only those components of the vector  $X_t$  that correspond to landmark positions.

Simulating  $X$  conditional on  $(V_0, V_T)$  is challenging for several reasons:

- (1) Contrary to many papers on diffusion bridge simulations, the conditioning is not on the full state, but on a subspace.
- (2) In the AHS-model, the diffusion coefficient  $\sigma$  is state-dependent.
- (3) The dimension of the driving Brownian motion  $W$  does not equal the dimension of the state space of the diffusion.
- (4) In the TV-model, the regularity of the paths of landmark locations and momenta is not the same (hypo-ellipticity).

In this section we demonstrate how these challenges can be dealt with following the approach, outlined in [36, 40, 8, 28]. In these papers, methods for simulation of conditioned diffusions using *guided proposals* were presented.

**3.1. Conditioned diffusions.** Throughout, we will assume that  $X$  admits smooth transition densities  $p$ , such that  $\mathbb{P}(X_t \in dy \mid X_s = x) = p(s, x; t, dy)$  for  $s < t$ . In this section, we consider the problem of simulating the diffusion process  $X$  conditioned on

$$X_0 = x_0 \quad \text{and} \quad V_T = v_T, \tag{15}$$

where  $V_T \sim N(L_T X_T, \Sigma)$ . This is different from the conditions in (14). Considering the initial state fully observed turns out to be an important step in the algorithms that we present. The diffusion conditioned on the events specified in (15) is rather loosely referred to as a bridge process (as it bridges available observations on the state of the process at times 0 and  $T$ ). An important result is that the bridge process satisfies an SDE that is similar to that of  $X$  but with an additional *guiding* term superimposed on the drift (this can be obtained by either using Doob's  $h$ -transform ([35]) or the theory of enlargement of initial filtration ([20, 5])). We denote the bridge process by  $X^* = (X_t^*, t \in [0, T])$  and define it as the strong solution to the SDE

$$dX_t^* = b(t, X_t^*) dt + a(t, X_t^*) r(t, X_t^*) dt + \sigma(t, X_t^*) dW_t, \quad X_0^* = x_0, \quad (16)$$

where  $a = \sigma\sigma'$  and  $r(t, x) = \nabla_x \log \rho(t, x)$ ,  $t \in [0, T]$ ,  $x \in \mathbb{R}^N$ . For specifying  $\rho$ , let  $(f_1, \dots, f_m)$  denote an orthonormal basis of  $\text{Col}(L_T')$ , and let  $(f_{m+1}, \dots, f_N)$  denote an orthonormal basis of  $\ker(L_T)$ . Suppose  $x = \sum_{i=1}^N \xi_i f_i$  is such that  $L_T x = v_T$ . This is equivalent to

$$\sum_{i=1}^m \xi_i L_T f_i = v_T, \quad (17)$$

where the equality follows since  $f_{m+1}, \dots, f_d \in \ker L_T$ . If we fix  $\xi_1, \dots, \xi_m$  by (17), then  $\rho$  is defined by

$$\rho(t, x) = \int_{\mathbb{R}^{N-m}} p\left(t, x; T, \sum_{i=1}^N \xi_i f_i\right) d\xi_{m+1}, \dots, d\xi_N. \quad (18)$$

We refer to this form of  $\rho$  as *exact matching*. This exact matching is a limiting case of *inexact matching*, where we take  $\Sigma$  to be any invertible matrix and have

$$\rho(t, x) = \int_{\mathbb{R}^N} p(t, x; T, \xi) \psi(v_T; L_T \xi, \Sigma) d\xi, \quad (19)$$

with  $\psi(x; \mu, \Sigma)$  denoting the density of the  $N(\mu, \Sigma)$ -distribution, evaluated at  $x$  and  $\xi = [\xi_1 \ \xi_2 \ \dots \ \xi_N]'$ . The limiting case of exact matching follows upon taking  $\Sigma = \varepsilon^2 I$  and  $\varepsilon \downarrow 0$ .

**Remark 1.** The solution of equation (16) with (19) implies that  $X_T^*$  has density

$$\eta(\xi; x_0) = \frac{p(0, x_0; T, \xi) \psi(v - L_T \xi; \Sigma) d\xi}{\int p(0, x_0; T, \xi) \psi(v - L_T \xi; \Sigma) d\xi}. \quad (20)$$

A derivation is given in the appendix in [28]. This equation reveals a nice Bayesian interpretation: a sample from  $X^*$  is obtained in two steps:

- (1) Consider the statistical model where we observe a realisation  $v_T$  from  $V_T \sim N(L_T \xi, \Sigma)$ . Here  $\Sigma$  is assumed to be known. Endow the parameter  $\xi$  with a prior distribution that has density  $\pi(\xi) = p(0, x_0; T, \xi)$  (with respect to Lebesgue measure on  $\mathbb{R}^N$ ). Sample from the posterior of  $\xi$ , that is, from the distribution of  $\xi$  conditional on  $V_T = v_T$  (the density of the posterior is  $\eta$ ).
- (2) Simulate the diffusion starting at  $x_0$  conditioned to hit  $\xi$  at time  $T$ .

**Remark 2.** Within Bayesian statistics it is common to write the data-generating model in a hierarchical way. For inexact matching the hierarchical scheme is as follows:

$$\begin{aligned} v_T | x_T &\sim N(L_T x_T, \Sigma_T) \\ v_0 | x_0 &\sim N(L_0 x_0 + \Sigma_0) \\ x_T | x_0 &\sim p(0, x_0; T, x_T) \\ x_0 &\sim \pi(x_0), \end{aligned}$$

where  $\pi$  denotes the prior density on the initial state. The observed variables are  $v_0$  and  $v_T$ ; the unobserved variables are  $x_0$  and  $x_T$ . Bayesian inference is based on the distribution of unobserved variables, conditional on observed variables. Hence (using Bayesian notation)

$$\begin{aligned} p(x_0, x_T | v_0, v_T) &\propto p(v_0, v_T | x_0, x_T) p(x_0, x_T) \\ &= p(v_0 | x_0) p(v_T | x_T) p(0, x_0; T, x_T) \pi(x_0) \\ &\propto p(v_0 | x_0) \pi(x_0) \eta(x_T; x_0), \end{aligned}$$

where  $\eta$  is as in Equation (20). Because the transition density is intractable,  $\eta$  is intractable. Simulation of  $X^*$  simply means that  $\eta$  is obtained as the marginal law of  $X^*$  at time  $T$ , as shown in Remark 1. This explains that the guiding term in  $X^*$  is targeting the correct distribution.

**Remark 3.** In all our numerical implementations we take  $\Sigma = \varepsilon I$  for two reasons: (i) taking  $\varepsilon$  small but strictly positive enhances numerical stability; (ii) from a practical point of view, as landmarks are often annotated manually, it is a realistic assumption that some error is induced, reflected by a larger value of  $\varepsilon$ .

**Remark 4.** For the AHS-model, the density  $p$  may not be smooth on the entire state space. We conjecture that the smoothness assumption that we impose on  $p$  is stronger than actually needed, and smoothness of  $\rho$  as defined in either (18) or (19) is sufficient.

### 3.2. Guided proposals.

3.2.1. *Introduction.* Since the transition densities of a diffusion are only available in closed form in very special cases,  $\rho$  in (19) is intractable. This prevents using a numerical discretisation scheme on the SDE for  $X^*$ , where the process would be simulated forward on a fine grid (for example using Euler's method). The key idea of [36] consists of instead simulating from a process  $X^\circ$  that is obtained by replacing  $p$  by the transition densities  $\tilde{p}$  of an auxiliary diffusion process  $\tilde{X}$  for which  $\tilde{p}$  is tractable. This is naturally the case for linear processes  $\tilde{X}$  whose dynamics are governed by the SDE

$$d\tilde{X}_t = \tilde{b}(t, \tilde{X}_t) dt + \tilde{\sigma}(t) dW_t, \quad (21)$$

where  $\tilde{b}$  is of the form

$$\tilde{b}(t, x) = \tilde{\beta}(t) + \tilde{B}(t)x. \quad (22)$$

Hence, instead of sampling from  $X^*$ , one samples from  $X^\circ$  defined by

$$dX_t^\circ = b(t, X_t^\circ) dt + a(t, X_t^\circ) \tilde{r}(t, X_t^\circ) dt + \sigma(t, X_t^\circ) dW_t, \quad X_0^\circ = x_0, \quad (23)$$

with  $\tilde{r}(t, x) = \nabla_x \log \tilde{\rho}(t, x)$ , where  $\tilde{\rho}$  is derived from  $\tilde{p}$  exactly as  $\rho$  is in terms of  $p$ . We call  $t \mapsto a(t, X_t^\circ) \tilde{r}(t, X_t^\circ)$  the *guiding term*, as it is a term that is superimposed on the

drift of the original SDE for  $X$  to satisfy the imposed conditioning at time  $T$ . Draws from this *guided diffusion bridge proposal* can subsequently be accepted/rejected in a Metropolis-Hastings sampler, provided that

- (1) the law of  $X^*$  is absolutely continuous with respect to the law of  $X^\circ$ ;
- (2) the Radon-Nikodym derivative is tractable, with the unknown transition densities  $p$  only appearing as multiplicative constant.

We will explain shortly that these requirements set some restrictions on  $\tilde{b}$  and  $\tilde{\sigma}$ , which can fortunately be satisfied for both the TV and AHS-model. An implicit assumption made throughout is that a strong solution to the SDE in (23) exists.

3.2.2. *Notation.* For easy reference, the following table summaries and introduces some notation. The rightmost three columns give the drift, diffusion coefficient and measure on  $C([0, T], \mathbb{R}^N)$  respectively.

$X$	original, unconditioned diffusion process, defined by (13)	$b$	$\sigma$	$\mathbb{P}$
$X^*$	corresponding bridge, conditioned on $v$ , defined by (16)	$b^*$	$\sigma$	$\mathbb{P}^*$
$X^\circ$	proposal process defined by (23)	$b^\circ$	$\sigma$	$\mathbb{P}^\circ$
$\tilde{X}$	linear process defined by (21) with transition densities $\tilde{p}$ appearing in the definition of $X^\circ$	$\tilde{b}$	$\tilde{\sigma}$	$\tilde{\mathbb{P}}$

3.2.3. *Existence of guided proposals.* Guided proposals only exist if the auxiliary process is chosen such that  $\tilde{X}$  admits transition densities. For that, we recap some results from section 2.1 in [8]. Let  $\Phi(t)$  denote the fundamental matrix solution of the ODE

$$d\Phi(t) = \tilde{B}(t)\Phi(t) dt, \quad \Phi(0) = I,$$

set  $\Phi(t, s) = \Phi(t)\Phi(s)^{-1}$  and define  $L(t) = L_T\Phi(T, t)$ . Throughout, we will assume that the matrices  $L_T$ ,  $\tilde{B}$  and  $\tilde{a}$  are such that the matrix

$$\int_t^T \Phi(T, \tau)\tilde{a}(\tau)\Phi(T, \tau)' d\tau,$$

is strictly positive definite for  $t < T$ . This implies that the matrix

$$M^\dagger(t) := \int_t^T L(\tau)\tilde{a}(\tau)L(\tau)' d\tau \tag{24}$$

is also strictly positive definite for all  $t \in [0, T)$  and, in particular, invertible. For uniformly elliptic diffusions this will always be the case, but for hypo-elliptic diffusions this requires careful choice of  $(\tilde{B}, \tilde{\sigma})$ . We use the pseudo-inverse notation, as without noise on the observation at time  $T$ , we have  $M^\dagger(T) = 0$ , and the inverse is not defined.

It follows from lemma 2.5 in [8] that under the assumption that  $M^\dagger$  is strictly positive definite, nondegenerate transition densities  $\tilde{p}$  exist and

$$\tilde{r}(t, x) = L(t)'M(t)(v - \mu(t) - L(t)x), \quad t \in [0, T], \tag{25}$$

where

$$\mu(t) = \int_t^T L(\tau)\tilde{\beta}(\tau) d\tau, \tag{26}$$

and  $M(t) = [M^\dagger(t)]^{-1}$ .

3.2.4. *Matching conditions and absolute continuity.* For exact matching, absolute continuity will only hold if the parameters of the auxiliary process  $\tilde{X}$ , i.e.  $\tilde{B}$ ,  $\tilde{\beta}$  and  $\tilde{\sigma}$ , satisfy certain *matching conditions*. This is also relevant for inexact matching as it contains exact matching as a limiting case. Under these matching conditions, a key result from [8] states that  $\mathbb{P}^* \ll \mathbb{P}^\circ$  (absolute continuity) and

$$\frac{d\mathbb{P}^*}{d\mathbb{P}^\circ}(X^\circ) = \frac{\tilde{\rho}(0, x_0)}{\rho(0, x_0)} \Psi(X^\circ),$$

where  $\rho$  is as defined in (18) and (19) (corresponding to exact and inexact matching respectively). In addition, we have

$$\Psi(X^\circ) = \exp\left(\int_0^T \mathcal{G}(s, X_s^\circ) ds\right), \quad (27)$$

$$\begin{aligned} \mathcal{G}(s, x) &= (b(s, x) - \tilde{b}(s, x))' \tilde{r}(s, x) \\ &\quad - \frac{1}{2} \text{tr}\left([a(s, x) - \tilde{a}(s)] [\tilde{H}(s) - \tilde{r}(s, x) \tilde{r}(s, x)']\right) \end{aligned}$$

and

$$\tilde{H}(s) = L(s)' M(s) L(s). \quad (28)$$

In case the diffusion is uniformly elliptic,  $L_T = I_{N \times N}$  and exact matching, then it was shown in [36] that  $\tilde{a} = \sigma\sigma'$  must satisfy  $\tilde{a}(T) = a(T, x_T)$  for absolute continuity. In the more general case considered here, the matching conditions look somewhat more difficult, a precise statement is given in section 2 of [8]. Especially for the AHS-model, these conditions are hard to verify (mainly due to the fact that the diffusivity is state dependent and not all components of  $X_T$  are observed). However, the results in this paper suggest that absolute continuity of  $\mathbb{P}^*$  with respect to  $\mathbb{P}^\circ$  is satisfied when

$$L_T b(T, X_T^\circ) = L_T \tilde{b}(T, X_T^\circ) \quad \text{and} \quad L_T a(T, X_T^\circ) L_T' = L_T a(T) L_T'. \quad (29)$$

This conjecture is numerically confirmed by experiments in Section 4.1 of [8]. By an appropriate choice of the auxiliary process  $\tilde{X}$ , we can assure both conditions in (29) to be satisfied for both the TV- and AHS-model (key to this is that in the AHS-model, the noise on the landmark positions does not depend on the unobserved momenta). Details are given in the next section.

3.2.5. *Computational aspects for computing the guiding term.* Computing the guiding term and  $\Psi_T(X^\circ)$  requires computing  $\tilde{L}(t)$ ,  $M(t)$  and  $\mu(t)$  for  $t \in [0, T]$ . This may at first sight seem cumbersome. However, it follows from Lemma 2.4 in [28] that  $L(t)$  satisfies the backward ordinary differential equation

$$dL(t) = -L(t) \tilde{B}(t) dt, \quad L(T) = L_T.$$

Numerically, we solve this equation by an implicit Euler scheme. In case of inexact matching,  $M^\dagger$  is given by  $M^\dagger(t) := \int_t^T L(\tau) \tilde{a}(\tau) L(\tau)' d\tau + \Sigma_T$  and henceforth satisfies the backwards ordinary differential equations

$$dM^\dagger(t) = -L(t) \tilde{a}(t) L(t)' dt, \quad M^\dagger(T) = \Sigma_T.$$

For exact matching the same equation applies, except that  $M^\dagger(T) = 0_{m \times m}$ . Hence,  $M(t)$  and  $\mu(t)$  can be approximated by a numerical quadrature rule using (24) and (26) respectively. In our implementation we have used the trapezoid rule for this purpose.

#### 4. GUIDED PROPOSALS FOR LANDMARK MODELS

Guided proposals are specified by choice of the auxiliary process  $\tilde{X}$ . Here we detail this choice for the three landmarks models considered. Recall (see also Equation (8))

$$\frac{\partial H}{\partial p_i} = \sum_{j=1}^n p_j k(q_i - q_j) \quad \text{and} \quad \frac{\partial H}{\partial q_i} = \sum_{j=1}^n \langle p_i, p_j \rangle \nabla k(q_i - q_j). \quad (30)$$

**4.1. Choice of auxiliary process for the MS- and TV-model.** In the MS-model we have

$$dq_i^\alpha = \frac{\partial H}{\partial p_i^\alpha} dt \quad \text{and} \quad dp_i^\alpha = -\lambda \frac{\partial H}{\partial p_i^\alpha} dt - \frac{\partial H}{\partial q_i^\alpha} dt + \gamma_i dW_t^i.$$

The matching conditions (29) suggest to match both the drift on the landmarks positions and the diffusivity at time  $T$ . In view of (30), we take the auxiliary process  $\tilde{X}$  as

$$d\tilde{q}_i^\alpha = \sum_{j=1}^n \tilde{p}_j k(q_i^T - q_j^T) dt \quad \text{and} \quad d\tilde{p}_i^\alpha = -\lambda \sum_{j=1}^n \tilde{p}_j k(q_i^T - q_j^T) dt + \gamma_i dW_t^i,$$

where  $q_i^T$  is the observed  $i$ -th landmark position at time  $T$ . Because the kernels are evaluated on the final positions, these equations define a linear process, from which  $\tilde{B}$ ,  $\tilde{\beta}$  and  $\tilde{\sigma}$  can be inferred directly.

**4.2. Choice of auxiliary process for the AHS-model.** As the matching assumptions are formulated for an SDE in Itô form, we first need to transform the AHS-model equations from Stratonovich to Itô form. To compute the additional term in the drift, we specify the noise kernels to be located at fixed positions. We suppose at location  $\delta_\ell$  kernel  $q \mapsto \sigma_\ell(q)$  with coordinates as specified in Equation (11).

**Proposition 1.** For the AHS-model, the additional term in the drift when switching from Stratonovich to Itô form for  $q$  is given by

$$\frac{1}{2} \sum_{\ell} z(q) \bar{k}_\tau(q - \delta) \gamma. \quad (31)$$

For  $p$  this term is given by

$$\frac{1}{2} \sum_{\ell} \langle p, \gamma \rangle (z(q) \nabla \bar{k}_\tau(q - \delta) - \bar{k}_\tau(q - \delta) \nabla z(q)). \quad (32)$$

Here, in the notation we have omitted dependence of  $(\tau, \delta, \gamma)$  on  $\ell$  and have denoted

$$z(q) = \langle \nabla \bar{k}_\tau(q - \delta), \gamma \rangle.$$

This proposition shows that there is a simple way to take the Stratonovich-Itô correction into account in the drift of the auxiliary process  $\tilde{X}$ : for landmark  $i$  one superimposes the terms (31) and (32) to the drift of the auxiliary process for the TV-model, with the final positions  $q = q_i^T$  substituted.

For the diffusion coefficient, it is important to match the diffusivity in the landmark positions at time  $T$ . This can be accomplished by replacing  $\sigma_\ell(q_i)$  in equation (12) by  $\sigma_\ell(q_i^T)$ . For the diffusivity appearing in the equation for  $p_i$  we have more flexibility. In the numerical examples we have chosen to approximate  $p_i \cdot \sigma_\ell(q_i)$  by  $m_i \cdot \sigma_\ell(q_i^T)$  with  $m_i = 0$  initially. Then, at iterations  $k \times 20$ , with  $k = 1, \dots, 5$  we update  $m_i$  by the momentum vector for landmark  $i$  at time  $T$  of the most recently simulated guided proposal (here “iteration” refers to one step of the MCMC-algorithm presented in Section 5). While not strictly necessary, we anticipate this yields improved guided proposals (in the sense that the paths better resemble true conditioned diffusion paths) compared to fixing  $m_i = 0$  throughout. As this is an instance of an adaptive MCMC scheme, we ensure diminishing adaptation by fixing the auxiliary process after a given number of iterations.

## 5. MCMC ALGORITHMS FOR LANDMARK MATCHING

Both the drift  $b$  and the diffusion coefficient  $\sigma$  in (13) may contain unknown parameters. Suppose the vector of unknown parameters is  $\theta$  so we will write  $b_\theta$  and  $\sigma_\theta$ . In this section we present an MCMC (Markov Chain Monte Carlo) algorithm to draw from  $(X, \theta)$  conditional on  $(v_0, v_T)$  (recall that  $X = (X_t, t \in [0, T])$  is the “full path”). It is well known that in case of unknown parameters in the diffusion coefficient, a Gibbs sampler that successively update  $\theta | X$  and  $X | \theta$  lead to an invalid (reducible) scheme (cf. [33]). To circumvent this problem, the essential idea is to update Wiener increments  $W$  rather than the process  $X$  itself. The outlined algorithm below follows the exposition in [40]. As we have made the assumption that a strong solution to the SDE (23) exists, there is a measurable map  $\mathcal{GP}_\theta$  such that  $X^\circ = \mathcal{GP}_\theta(x_0, W)$ , where  $W$  is the driving Wiener process in  $\mathbb{R}^{N'}$  ( $\mathcal{GP}$  being an abbreviation of *Guided Proposal*).

**5.1. Bridging two landmark configurations.** In this section we consider the case, where the landmark positions are observed at times 0 and 1 with additive Gaussian noise. Denote these observations by  $v_0$  and  $v_T$  respectively. Let  $x_0 = (q_0, p_0)$  and  $x_T = (q_T, p_T)$  denote the latent states.

We propose a Gibbs sampler for updating  $(W, \theta, p_0, x_T)$  that is initialised by choosing initial values for  $p_0$  and  $\theta$ , setting  $x_0 = [v_0; p_0]$ , drawing Wiener increments  $W$  and computing  $X = \mathcal{GP}_\theta(x_0, W)$ . The sampler cycles over the steps

- (1) sample  $(W, X)$  conditional  $(v_0, p_0, \theta, v_T)$  using guided proposals, with pCN (pre-conditioned Crank-Nicolson) updates on the Wiener increments;
- (2) sample  $p_0$  conditional on  $(v_0, \theta, W, v_T)$  using MALA (Metropolis Adjusted Langevin Algorithm), with gradients obtained using automatic differentiation;
- (3) sample  $\theta$  conditional on  $(v_0, p_0, W)$ .

This is along the lines of the algorithm proposed in section 5 of [28]. Note that step 1 also updates  $p_T$  automatically. Note that we in this case do not update the initial landmark positions; assuming these are observed accurately (so that  $v_0$  and  $q_0$  are about the same). Each of the 3 steps is made precise in Algorithms 1–3 below. As  $\theta$  is part of the sampler, we add a subscript  $\theta$  in our notations to denote possible dependence on  $\theta$ . For example, we write  $\Psi_\theta(X)$ , where  $\Psi$  is as defined in (27).

We denote prior densities on  $\theta$ ,  $q_0$  and  $p_0$  generically by  $\pi$  (Bayesian notation).

**Algorithm 1** (Update  $(W, X)$ , conditional on  $(v_0, p_0, \theta, v_T)$ ). Choose a persistence parameter  $\eta \in [0, 1]$ . Set  $x_0 = [v_0; p_0]$

- Compute  $L_\theta(t)$ ,  $M_\theta^\dagger(t)$  and  $\mu_\theta(t)$  for  $t \in [0, T]$ .
- Sample a Wiener process  $Z$ , independently of  $W$  and set

$$W^\circ = \eta W + \sqrt{1 - \eta^2} Z.$$

Compute  $X^\circ = \mathcal{GP}_\theta(x_0, W^\circ)$ .

- Compute

$$A = \Psi_\theta(X^\circ) / \Psi_\theta(X).$$

Draw  $U \sim \mathcal{U}(0, 1)$ . If  $U < A$  set  $X = X^\circ$  and  $W = W^\circ$ .

**Algorithm 2** (Update  $p_0$ , conditional on  $(v_0, \theta, W, v_T)$ ). Choose a step-size  $\delta > 0$ .

- Sample  $Z \sim N_{dn}(0, I)$  (with  $d$  the dimension of a landmark). Set  $x_0 = [v_0; p_0]$  and propose

$$p_0^\circ = p_0 + \frac{\delta}{2} \mathcal{L}_\theta(x_0, W) + \sqrt{\delta} Z,$$

where

$$\mathcal{L}_\theta(x_0, W) = \nabla_{p_0} \left( \log \Psi_\theta(\mathcal{GP}_\theta(x_0, W)) + \log \tilde{\rho}_\theta(0, x_0) \right).$$

Here, the gradient is obtained by automatic differentiation. Set  $x_0^\circ = [v_0; p_0^\circ]$ .

- Compute  $X^\circ = \mathcal{GP}_\theta(x_0^\circ, W)$  and  $\mathcal{L}_\theta(x_0^\circ, W)$ .
- Compute

$$A = \frac{\Psi_\theta(X^\circ) \tilde{\rho}_\theta(0, x_0^\circ) \pi(p_0^\circ) \psi(p_0; p_0^\circ + \delta \mathcal{L}_\theta(x_0^\circ, W) / 2, \delta I)}{\Psi_\theta(X) \tilde{\rho}_\theta(0, x_0) \pi(p_0) \psi(p_0^\circ; p_0 + \delta \mathcal{L}_\theta(x_0, W) / 2, \delta I)}.$$

Draw  $U \sim \mathcal{U}(0, 1)$ . If  $U < A$  set  $X = X^\circ$  and  $p_0 = p_0^\circ$ .

**Algorithm 3** (Update  $\theta$ , conditional on  $(v_0, p_0, W)$ ). Choose an irreducible Markov kernel  $q$  on the domain of  $\theta$ . Set  $x_0 = [v_0; p_0]$

- Sample  $\theta^\circ$  from a kernel  $q(\cdot | \theta)$ .
- Compute  $X^\circ = \mathcal{GP}_{\theta^\circ}(x_0, W)$ .
- Compute

$$A = \frac{\Psi_{\theta^\circ}(X^\circ) \tilde{\rho}_{\theta^\circ}(0, x_0) \pi(\theta^\circ) q(\theta | \theta^\circ)}{\Psi_\theta(X) \tilde{\rho}_\theta(0, x_0) \pi(\theta) q(\theta^\circ | \theta)}.$$

Draw  $U \sim \mathcal{U}(0, 1)$ . If  $U < A$  set  $X = X^\circ$  and  $\theta = \theta^\circ$ .

**5.2. RMMALA proposals on the initial state.** We also consider the case where multiple shapes are observed and the primary aim is to estimate the initial state which is then considered as template shape. Especially with a large number of landmarks simple random-walk updates will perform terribly bad as these do not respect the geometry of the landmark configuration. For that reason we will use the RMMALA (Riemannian Manifold Metropolis Adjusted Langevin Algorithm) as introduced in Section 5 of [13]. Denote the initial state  $i$  by  $x_0 = (q_0, p_0)$ . Suppose we have  $I$  landmark configurations and for the  $i$ -th configuration  $X^i = \mathcal{GP}_\theta(x_0, W^i)$ . Assume  $(\theta, W^1, \dots, W^I)$  is fixed and no landmark configuration is observed at time zero.

**Algorithm 4** (Update initial landmark positions  $q_0$ , conditional on  $(p_0, v_T, \theta, W^1, \dots, W^I)$ ). Choose a step-size  $\delta > 0$ .

- Sample  $Z \sim N_{dn}(0, K(q))$ , where  $K(q)$  is the matrix with blocks  $K(q)_{ij} = K(q_i, q_j)$ ,  $1 \leq i \leq n$ . Propose

$$q_0^\circ = q_0 + \frac{\bar{\delta}}{2} K(q_0) \mathcal{L}(q_0) + \sqrt{\bar{\delta}} Z,$$

where

$$\mathcal{L}(q_0) := \nabla_q \left( \log \tilde{\rho}_\theta(0, (q_0, p_0)) + \sum_{i=1}^I \log \Psi_\theta(g((q_0, p_0), W^i)) \right).$$

Here, the gradient is obtained by automatic differentiation. Set  $x_0^\circ = (q_0^\circ, p_0)$ .

- For  $i = 1, \dots, I$ , compute  $X^{\circ, i} = \mathcal{GP}_\theta(x_0^\circ, W^i)$  and  $\mathcal{L}_\theta(q_0^\circ)$ .
- Compute

$$A = \frac{\tilde{\rho}_\theta(0, x_0^\circ) \pi(q_0^\circ) \psi(q_0; q_0^\circ + \delta K(q_0^\circ) \mathcal{L}(q_0^\circ)/2, \delta K(q_0^\circ))}{\tilde{\rho}_\theta(0, x_0) \pi(q_0) \psi(q_0; q_0 + \delta K(q_0) \mathcal{L}(q_0)/2, \delta K(q_0))} \prod_{i=1}^I \frac{\Psi_\theta(X^{\circ, i})}{\Psi_\theta(X^i)}.$$

Draw  $U \sim \mathcal{U}(0, 1)$ . If  $U < A$  set  $X = X^\circ$  and  $q_0 = q_0^\circ$ .

## 6. NUMERICAL EXAMPLES

**6.1. Settings.** Before presenting examples we discuss precise settings in the numerical experiments.

**6.1.1. Specification of Hamiltonian kernel.** We take a Gaussian kernel  $K$  of the form  $K(x) = k(x) \text{Id}_d$  with

$$k(x) = c \exp(-\|x\|^2/(2a^2)).$$

Note that  $\nabla k(x) = -c a^{-2} k(x) x$ .

**6.1.2. Specification of the noise.** For the TV-model, we take the noise on all landmarks the same, i.e.  $\sigma_i = \gamma$  for all  $i \in \{1, \dots, n\}$ .

For the AHS-model, let  $\tau > 0$ . We take the noise fields centred at points that are both horizontally and vertically separated by a distance that is an integer multiple of  $2\tau$ . Denote the locations of the noise fields by  $\{\delta_j\}$ . At each location  $\delta_j$  we take noise fields to be

$$\frac{2}{\pi} \gamma \bar{k}_\tau(x - \delta_j) \begin{bmatrix} 1 \\ 0 \end{bmatrix} \quad \text{and} \quad \frac{2}{\pi} \gamma \bar{k}_\tau(x - \delta_j) \begin{bmatrix} 0 \\ 1 \end{bmatrix},$$

where we fix  $\bar{k}_\tau(x) = \exp(-\|x\|^2/(2\tau^2))$ . This kernel is similar to the Hamiltonian kernel, but does not have to be so in general. The scaling by  $2/\pi$  is chosen so that if  $\gamma = 1$  the noise on the landmarks positions is close to 1 uniformly in space (close to a decomposition of unity).

**6.1.3. Specification of parameter  $\theta$ .** In the simulations, we fix the scaling parameter  $\tau$  of the noise-kernels, as well as their positions. We estimate the scaling parameters  $c$  and  $a$  appearing in the Hamiltonian kernel, as well as the size (amplitude) of the noise ( $\gamma$ ). Hence,  $\theta = (a, c, \gamma)$ . In the TV-model we take the damping coefficient  $\lambda$  equal to zero (note that the approaches in [27] requires  $\lambda$  to be strictly positive though small).

6.1.4. *Prior on the landmark positions and momenta.* In the problem of bridging two landmark configurations we use a prior on the landmark momenta similar to the prior suggested in Section 3 of [27]. More specifically, we take

$$\begin{aligned}\pi(q_1, \dots, q_n, p_1, \dots, p_n) &= \pi(p_1, \dots, p_n \mid q_1, \dots, q_n) \pi(q_1, \dots, q_n) \\ &= \psi(p_1, \dots, p_n; 0, \kappa K(q)^{-1}) \prod_{i=1}^n \psi(q_i; 0, \kappa_{\text{position}}).\end{aligned}$$

As we assumed that the landmark positions are observed, we make the shortcut where we assume  $(p_1, \dots, p_n) \sim N(0, \kappa K(q)^{-1})$ , where  $\{q_i\}$  are the observed landmark positions. Here,  $\kappa$  is a parameters that we fix to a large value.

6.1.5. *Tuning parameters for the MCMC-sampler.* As can be seen from algorithms 1 to 3, the proposed MCMC-algorithm requires specification of

- the persistence parameter  $\eta \in [0, 1]$  (Algorithm 1);
- the step size  $\delta > 0$  (Algorithm 2);
- the Markov kernel  $q$  for updating  $\theta$  (Algorithm 3).

Naturally, these choices affect the efficiency of the algorithm to explore the support of the target distribution. We target acceptance rates of about 50%. For the Markov kernel  $q$ , each component of  $\theta$  is positive and this is taken into account by using updates of the form  $\log \theta_i^\circ \mid \theta_i \sim N(\log \theta_i, \sigma_\theta^2)$ .

We adaptively tuned  $(\eta, \delta)$  to target an acceptance rate of 50% using the rule proposed in Section 3 of [34]. More precisely, every 20 iterations we either add or subtract  $\zeta(j)$  to  $\log(\eta/(1-\eta))$ ,  $\log \delta$  and  $\log \sigma_\theta^2$  with  $j$  denoting the iteration number. We took  $j \mapsto \zeta(j) = \min(0.2, 10/j)$ . A large number of landmarks may force  $\rho$  to be tuned close to 1 and for that reason in case of more than 10 landmarks we randomly choose 10 landmarks for which Wiener increments are updated (keeping the remaining increments fixed). We discretised guided proposals in time by taking a regular grid on  $[0, 1]$  with mesh-width 0.01, followed by applying the map  $s \mapsto s(2-s)$  to this grid (see also Section 5 on [40] for discretisation of guided proposals). Finally, in each example we chose  $\Sigma = \epsilon^2 I$  with  $\epsilon = 0.01$  (cf. Equation (19)), except for Example 1 and the experiment leading to Figure 8.

6.2. **Examples.** The source code of the numerical examples is available together with a Julia package `BridgeLandmarks` for shape analysis with stochastic landmark dynamics, [41]. Automatic differentiation was implemented via [32]. All computations were done on a MacBook Pro, with a 2.7GHz Intel Core i5 with 8 GB RAM.

**Example 1.** *1D landmarks.*

In Figure 3 we illustrate the matching problem with 3 landmarks in dimension 1. Here, the initial locations of the points are given by 0.5, 1.0 and 1.3 and we condition on  $e^{0.5}$ ,  $e^1$  and  $e^{1.3}$  respectively. We initialised the momentum to be 12,  $-15$ ,  $-15$  for landmarks 1, 2 and 3 respectively, forcing the lower paths to move towards the middle path. We consider both the TV- and AHS-model with fixed parameters set to  $a = 0.2$ ,  $c = 0.2$  and  $\gamma = 2.0$ . For the AHS-model, noise sources were positioned at  $\pm 1.5 i$  (with  $i$  integer-valued) and  $\tau = 0.75$ . We ran an algorithm composed of alternating one step of Algorithm 1 (bridge updating) and one step of Algorithm 2 (initial momenta updating) for 100 iterations. We took  $\eta_{\text{init}} = 0.9$  (appearing in the pCN updates in Algorithm 1),

$\epsilon = 0.001$ ,  $\delta_{\text{init}} = 0.1$  (in case of TV-model),  $\delta_{\text{init}} = 0.5$  (in case of AHS-model) and  $\kappa = 100$ .

**Example 2.** *Configurations in 2D.*

Moving to landmarks in  $\mathbb{R}^2$ , we start with  $n$  landmarks on the ellipse parametrised by  $(2 \cos(t), \sin(t))$ . The coordinates are obtained by taking  $t = 2\pi k/n$ ,  $k = 1, \dots, n$ . We consider a second shape that is obtained by mapping each landmark position  $q$  to

$$\begin{bmatrix} 1.2 \cos(\theta) & -\sin(\theta) \\ \sin(\theta) & 0.8 \cos(\theta) \end{bmatrix} q + \begin{bmatrix} 0.5 \\ 0 \end{bmatrix},$$

where we took  $\theta = \pi/4$ . This corresponds to rotating followed by stretching and translating the landmark positions. In the numerical experiments we fix the parameters  $(a, c, \gamma)$  and only update bridges and initial momenta. We took  $n = 18$  landmarks and show results for both the TV and AHS-model with the following settings:

Model	$a$	$c$	$\gamma$	$\eta_{\text{init}}$	$\epsilon$	$\delta_{\text{init}}$	$\kappa$
TV	0.273	0.20	2.0	0.9	0.01	0.1	100
AHS	0.273	0.02	0.2	0.9	0.01	0.1	100

The choice of  $a$  (Hamiltonian kernel parameter) corresponds to half the average distance between adjacent landmarks on the shape. The other parameters  $(c, \gamma)$  were chosen using visualisations of the generated bridges as (subjective) guidance.

The parameter  $\delta$  is the step size used in MALA updates for the initial momenta. The meaning of parameter  $\epsilon$  is explained in Remark 3. While possible, we advice against taking  $\epsilon$  exactly equal to zero as this choice yields numerical problems. Too small values can potentially be problematic for the AHS-model in particular, as the quality of the constructed guided proposals is worse for that model compared to those for the TV-model. Especially at early iterations this may cause numerical instability which can be overcome easily by relaxing the constraint imposed by the conditioning, i.e. taking a small positive value for  $\epsilon$  such as 0.01.

We ran the MCMC-sampler for 500 iterations, only updating initial momenta and Wiener increments. Visualisations from the output of the algorithms for the TV-model are in Figures 4, 5, 6 and 7. Computing time for the 500 iterates was about 6 minutes. From Figure 6 it is clear that the stationary region of the Markov chain is reached within 100 iterations. Also, from this figure it is clear that the sampled initial momenta push trajectories in the correct direction. For example, landmark number 13 is pushed eastwards. Figure 4 shows the time-evolution of landmark trajectories for a few iterations, showing no clear signs of early/late arrival. In Figure 5 bridges for all landmarks are overlaid, where each 10-th iterate is plotted. Finally, in Figure 7 we illustrate that our approach for adaptive tuning of parameters in the MCMC algorithm works satisfactory. For the AHS-model we took the noise specification as in Section 6.1.2 with  $\tau = 0.75$ ; the centers of the sources are depicted for example in Figure 16 (here, the radius of the circles equals  $\tau$ ).

In Appendix B we show the corresponding plots for the AHS-model (computing time about 38 minutes). In this case the Markov chain of initial momenta and bridges takes more iterations to reach its stationary regime. This can for example be seen from the right panel in Figure 17 in which iterates for the initial momentum vector is shown for 4 landmarks. In the leftmost panel of Figure 15 it can be seen that the initial

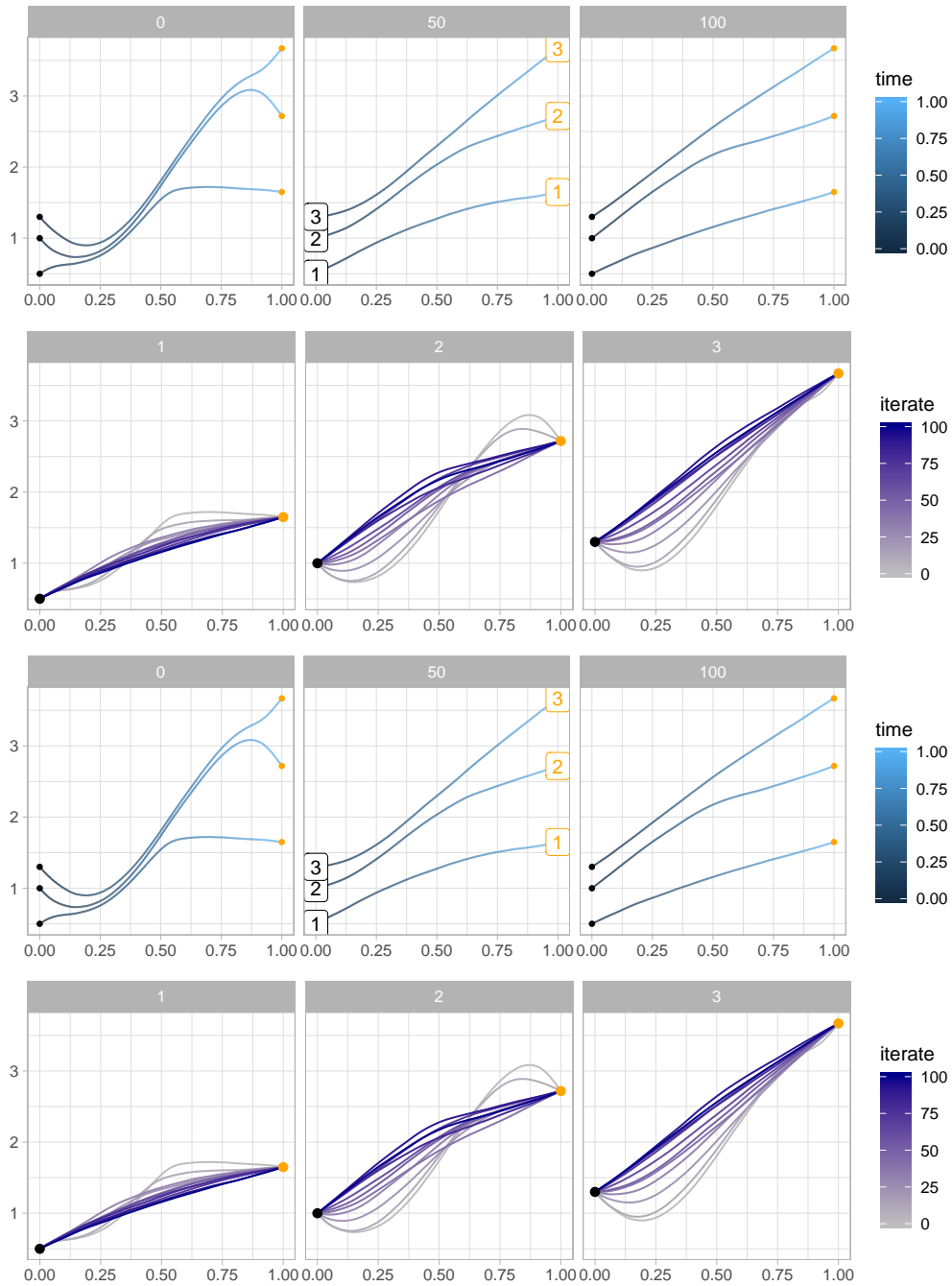


FIGURE 3. Simulation results for Example 1. Initial momenta at iteration 0 (initialisation of the algorithm) are 12,  $-15$ ,  $-15$  for landmarks 1, 2 and 3 respectively, forcing the paths lower path to move towards the middle path. Top panel: facets are over iterations. Lower panel: facets are over each of the three landmarks.

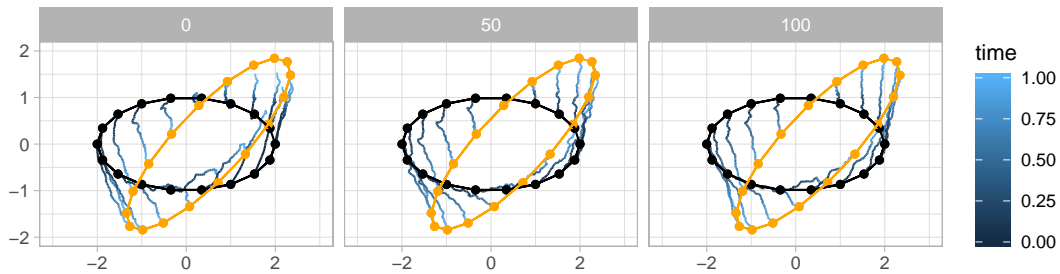


FIGURE 4. *Example 2, TV-model.* Initial shape (black) and final shape (orange) using 18 landmarks. The curves connecting corresponding black/orange landmarks are simulated bridges. The different panels correspond to three different iteration numbers. The colouring of the paths captures evolution of the trajectories over time. Note that the paths are smooth, as in the TV-model the noise is only in the momentum equation.

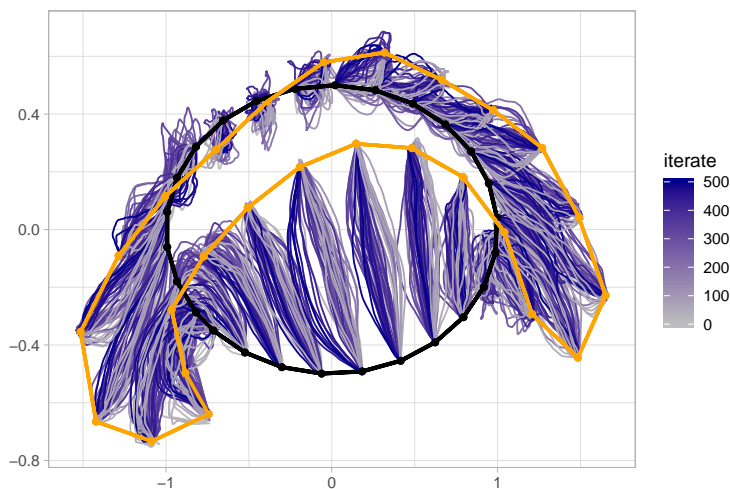


FIGURE 5. *Example 2, TV-model.* Initial shape (black) and final shape (orange) using 18 landmarks. Each 10-th curve is plotted over 500 iterations.

landmark bridges do not fully connect the sets of landmarks, especially in the top-right corner. This indicates that at early iterations sample paths of guided proposals deviate from paths from the AHS-model. This deviation gradually diminishes with increasing iteration index.

It is easy to incorporate inexact matching into the estimation procedure: all that needs to be done is specifying the matrix  $M^\dagger(T)$ . In Figure 8 we consider the TV-model just as before, but now we set  $\epsilon = 0.1$  for observing landmarks 10 up till 18 at end-time (so in this example, only the noise on the final configuration is heterogeneous). Inexact matching is clearly demonstrated in the right-hand panel.

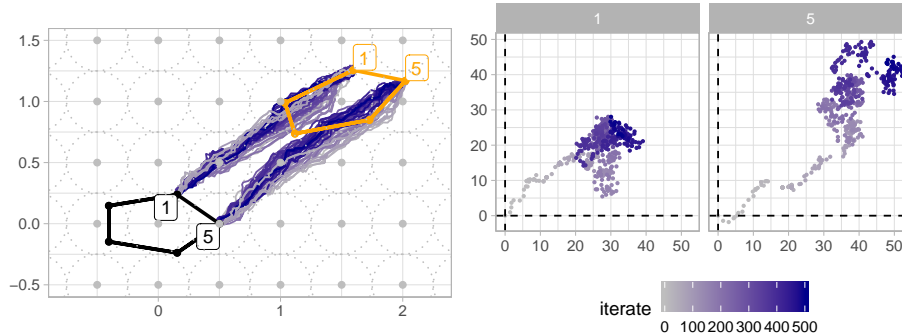


FIGURE 6. *Example 2, TV-model*. Left: as in Figure 5, but only showing paths for 18 chosen landmarks. Right: for each of these landmarks the iterates for the initial momentum vector is shown (each dot corresponding to one iteration).

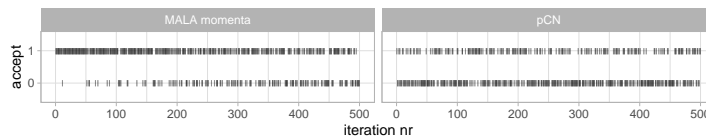


FIGURE 7. *Example 2, TV-model*. Iterates showing acceptance/rejection of updating the initial momenta (left panel) and Wiener increments (right panel). 1 corresponds to acceptance; 0 to rejection.

**Example 3.** Here we make a variation of Example 2 to illustrate that our method is capable of bridging shapes far apart. Here we consider the AHS-model, noting that similar good performance is obtained for the TV-model. In [2], poor performance was achieved when landmarks traverse multiple noise sources, because the scheme is challenged by high momentum coupled with high gradients in the  $p$ -equation of (12). To counter this, a linear approximation of the endpoint dynamics that involves numerical integration of derivatives of the flow dynamics was introduced. On the contrary, as can be seen from Figure 9, the methods discussed here are not challenged by multiple noise sources with high gradients, and the scheme works directly without the additional computationally demanding workaround. At early iterations, bridges have some difficulty to fully reach their corresponding landmark, but this is resolved at later iterations where the momenta pointing north-east become stronger.

**Example 4.** To illustrate results for rather different shapes (compared to an ellipse), we start from an ellipse and transform to landmarks representing points on the outline of a human corpus callosum. In total there are 26 landmarks. Here we used the TV-model with  $a$  (Hamiltonian kernel parameter) the average distance between adjacent landmarks

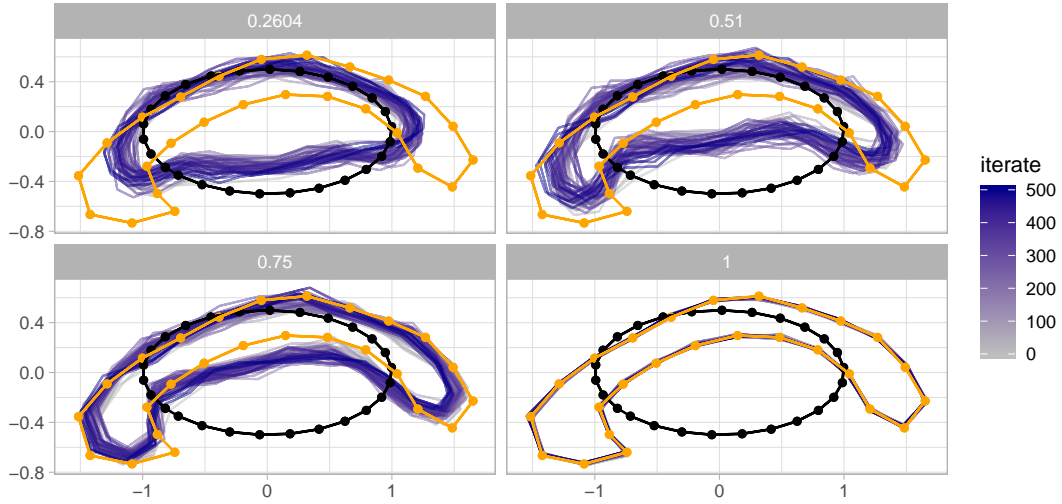


FIGURE 8. *Example 2, TV-model, inexact matching on half of the landmarks.* Initial shape (black) and final shape (orange) using 18 landmarks. Left and right panels: every 10th iteration at times 0.51 and 1 respectively. Clearly, there is inexact matching in the right part of the shape.

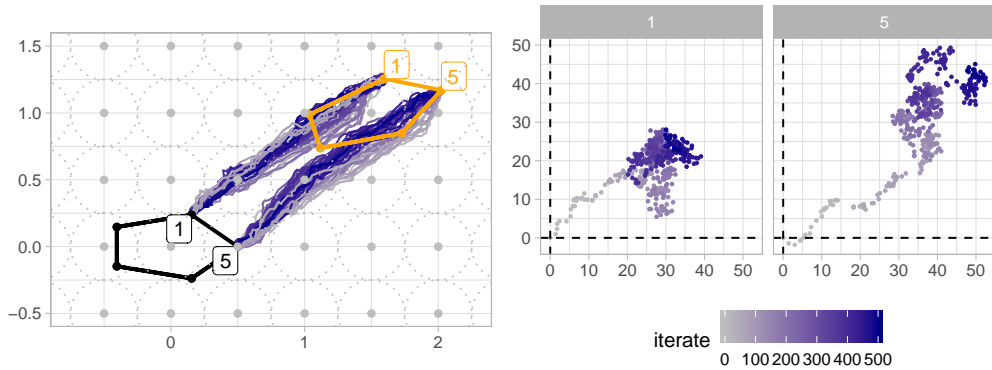


FIGURE 9. *Example 3, AHS-model.* Left: visualisation of bridges for 2 landmarks. Right: for each of these landmarks the iterates for the initial momentum vector is shown (each dot corresponding to one iteration).

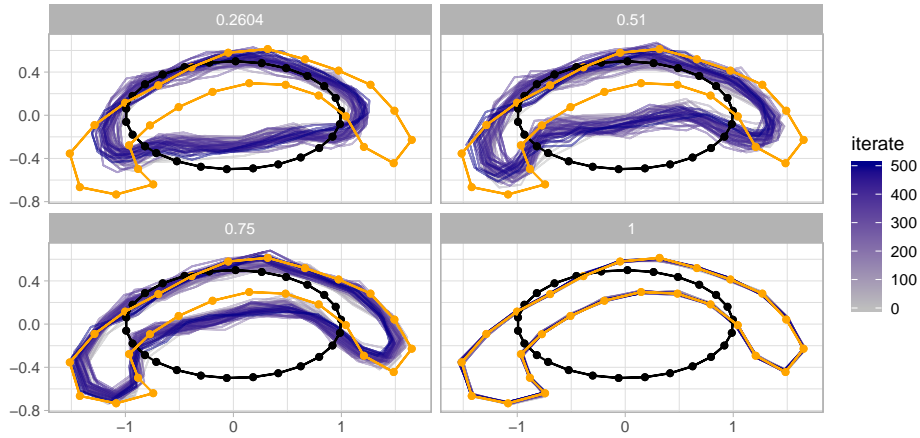


FIGURE 10. *Example 4, TV-model.* Initial shape (black) and final shape (orange) with 26 landmarks. Each panel corresponds to a fixed time. Within each panel every 10-th curve is plotted over 500 iterations.

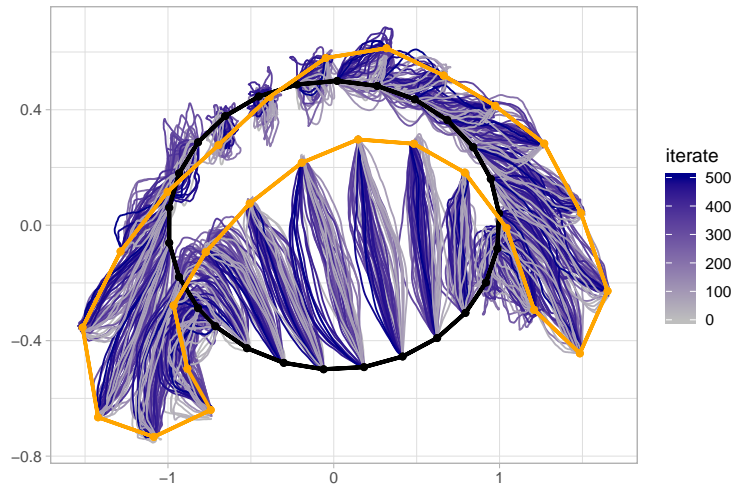


FIGURE 11. *Example 4, TV-model.* Initial shape (black) and final shape (orange) using 18 landmarks. Each 10-th curve is plotted over 500 iterations.

on the shape and  $(c, \gamma) = (0.2, 2.0)$ . In Figure 10 we show iterates at about 25%, 50%, 75% and 100% of the iterates (we chose times which are in the grid used for discretising the bridges). In Figure 11 we show trajectories of bridges over iterations.

**Example 5. Template estimation.**

Here, we simulate forward 10 trajectories using the TV-model. We took the initial configuration in an ellipse (exactly as in Example 2) using  $n = 15$  landmarks. In the forward

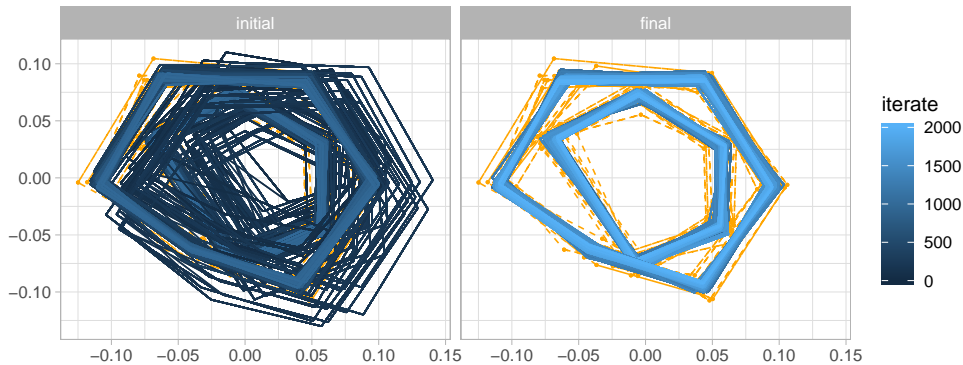


FIGURE 12. Initial shape configuration for Example 5 using the TV-model. The total number of iterates is split up over 2 panels. The true data-generating initial configuration is in red. The dashed orange curves are the 10 observed configurations. MCMC-iterates are shown in blue colours.

simulation we took  $(a, c, \gamma) = (2.0, 0.1, 0.7)$ . The 10 landmark configurations at time 1 were subsequently taken as data. In the MCMC estimation, we fix the initial momenta to be equal to zero but include parameter estimation. Hence, each MCMC-iteration consists of updating Wiener increments (determining the bridges), the parameter vector  $(a, c, \gamma)$  and the initial landmark positions. For the latter we used RMMALA (Algorithm 4 as detailed in Section 5.2). We initialised the step size with value 0.002. We ran the sampler for 2000 iterations, taking the discretisation grid,  $\epsilon$  and initialisation of  $a$  just as in Example 2. We used independent standard Exponential priors on  $a, c, \gamma$ . We deliberately initialised the template configuration incorrectly by taking one of the observed configuration and rotating and stretching the shape. This is done to illustrate that the Riemannian manifold MALA steps perform satisfactory. In any practical application one could initialise the template shape by one of the observed shapes.

Some results for the TV-model are shown in Figures 12 and 13. Clearly, the initial configuration can be recovered quite well, despite there are only 10 observed shapes. From the traceplots of the parameters it appears that both the Hamiltonian kernel parameter  $a$  and parameter  $c$  can be recovered well. It appears there is large uncertainty about  $\gamma$ . More generally, in the setting of estimation for discretely observed diffusions, accurate estimation of parameters in the diffusion coefficient tends to be harder than those appearing in the drift coefficient. It is not clear whether parameters within the various landmark models are identifiable at all, or that accurate identification of these parameters requires way more than 10 observed landmark configurations. Despite these issues, employing a prior on both  $c$  and  $\gamma$  and updating these parameters in the algorithm prevents fixing these to values which are incompatible with the observed landmark configurations.

**Example 6.** *Template estimation, cardiac data using the TV-model.*

In Figure 14 we show the results when applying the algorithm to landmarks on 14 cardiac images of human left ventricles [38]. The manually annotated landmarks are

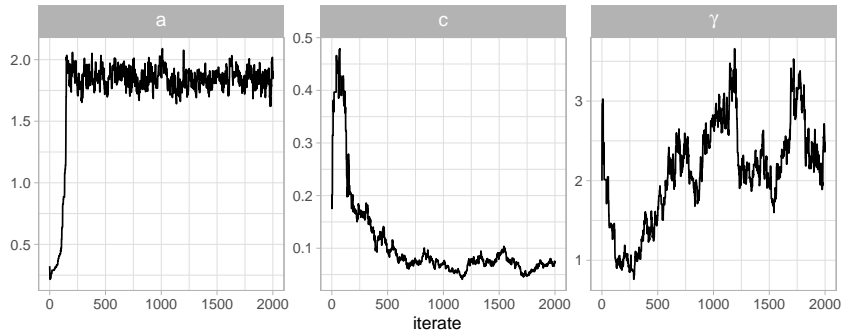


FIGURE 13. Trace plots of parameters for the experiment of Example 5 using the TV-model.

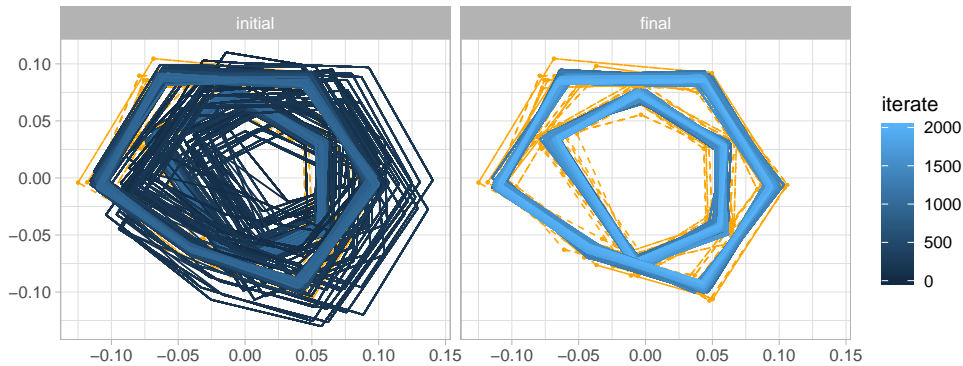


FIGURE 14. Cardiac data, Example 6. Iterates for initial landmark configuration. Result with downsampling to 14 landmarks (to reduce computing time, now 18 mins for 250 iterations).

consistently placed over the set of shapes. We selected 11 landmarks for each shape for the experiment with the goal of estimating the template shape and model parameters. The experiment extends the template estimation with Brownian motion performed in [37] to the models in focus in this paper. We used parameter updating, bridge updating and initial state updating (using RMMALA), while fixing the initial momenta to zero. We used 2000 iterations. From Figure 14 it appears that the chain reaches its stationary region after approximately 500 iterations. It is natural to extend this experiment to a larger set of landmarks. While this is possible, we prefer to postpone such an investigation to future research with emphasis on improving our algorithms to scale better with the dimension of the number of landmarks. Crucially, this presently depends on solving the backward equations detailed in Section 3.2.5 and on computing gradients by automatic differentiation used for updating the initial positions and/or momenta.

## 7. DISCUSSION AND FUTURE WORK

In this paper, we have extended the framework of [36, 8] for sampling diffusion bridges to nonlinear high dimensional stochastic Hamiltonian systems. For this work, some problems in computational anatomy [43] revolving around systems of particles to describe images have been our main motivation. We used these models throughout to illustrate the application of diffusion bridges specifically in stochastic landmark dynamics. We left open many possible improvements of this method such as allowing for multiple observations over time, resolving unknown landmark correspondence, a step towards infinite dimensional shape matching and the problem of the parametrisation of these shapes [6].

This work opens the door to not only a wider use in statistical inference in computational anatomy, but other related fields, where high dimensional stochastic Hamiltonian systems are involved in the modelling, such as in biology, data assimilation, swarming, etc. . . From a more theoretical point of view, various extensions of this work could be considered. The driving Brownian motion in the SDE could for example be generalised to a Lévy process or even rough paths.

From a numerical perspective, we used classical methods for simplicity, but the presented algorithms could be extended to include more modern numerical integration scheme or MCMC methods, such as geometric integrators [29, 14, 30, 17, 10], to preserve the geometrical structure of the problem, or some more advanced geometrical Hamiltonian Monte-Carlo methods [3, 4]. In addition, the use of automatic differentiation, similar as in [23, 24], has turned out to be beneficial for the implementation of efficient methods, and surely deserves to be more exploited for future works.

## ACKNOWLEDGEMENT

A substantial part of this research was carried out during a sabbatical leave of the second author at the University of Copenhagen (UCPH). Financial support by the faculty of Science, UCPH through the programme “Visiting scholars at SCIENCE” and by both the mathematics and computer science department of UCPH are greatly acknowledged. The work presented is in addition supported by the CSGB Centre for Stochastic Geometry and Advanced Bioimaging funded by a grant from the Villum foundation, and the Novo Nordisk Foundation grant NNF18OC0052000. AA acknowledge funding through EPSRC award EP/N014529/1 supporting the EPSRC Centre for Mathematics of Precision Healthcare at Imperial.

## REFERENCES

- [1] Alexis Arnaudon, Darryl D. Holm, Akshay Pai, and Stefan Sommer. A Stochastic Large Deformation Model for Computational Anatomy. In *Information Processing in Medical Imaging*, Lecture Notes in Computer Science, pages 571–582. Springer, 2017. ISBN 978-3-319-59049-3 978-3-319-59050-9. doi: 10.1007/978-3-319-59050-9\_45.
- [2] Alexis Arnaudon, Darryl D. Holm, and Stefan Sommer. A Geometric Framework for Stochastic Shape Analysis. *Foundations of Computational Mathematics*, 19(3): 653–701, June 2019. ISSN 1615-3383. doi: 10.1007/s10208-018-9394-z.

- [3] Alessandro Barp, François-Xavier Briol, Anthony D Kennedy, and Mark Girolami. Geometry and dynamics for markov chain monte carlo. *Annual Review of Statistics and Its Application*, 5:451–471, 2018.
- [4] Alessandro Barp, Anthony Kennedy, and Mark Girolami. Hamiltonian monte carlo on symmetric and homogeneous spaces via symplectic reduction. *arXiv preprint arXiv:1903.02699*, 2019.
- [5] Fabrice Baudoin. Conditioned stochastic differential equations: theory, examples and application to finance. *Stochastic Processes and their Applications*, 100(1-2):109 – 145, 2002. ISSN 0304-4149. doi: DOI:10.1016/S0304-4149(02)00109-6. URL <http://www.sciencedirect.com/science/article/B6V1B-45FGYNB-1/2/6e7978f4a8cbde00d7002ed9c33a1681>.
- [6] Martin Bauer, Martins Bruveris, and Peter W Michor. Overview of the geometries of shape spaces and diffeomorphism groups. *Journal of Mathematical Imaging and Vision*, 50(1-2):60–97, 2014.
- [7] Alexandros Beskos, Omiros Papaspiliopoulos, Gareth O. Roberts, and Paul Fearnhead. Exact and computationally efficient likelihood-based estimation for discretely observed diffusion processes (with discussion). *Journal of the Royal Statistical Society: Series B (Statistical Methodology)*, 68(3):333–382, June 2006. ISSN 1467-9868. doi: 10.1111/j.1467-9868.2006.00552.x.
- [8] Joris Bierkens, Frank van der Meulen, and Moritz Schauer. Simulation of partial bridges for hypo-elliptic diffusions. *To appear in Advances in Applied Probability*, 2019.
- [9] Mogens Bladt, Samuel Finch, and Michael Sørensen. Simulation of multivariate diffusion bridges. *Journal of the Royal Statistical Society: Series B (Statistical Methodology)*, 78(2):343–369, March 2016. ISSN 1467-9868. doi: 10.1111/rssb.12118.
- [10] Evelyn Buckwar, Massimiliano Tamborrino, and Irene Tubikanec. Spectral density-based and measure-preserving abc for partially observed diffusion processes. an illustration on hamiltonian sdes. *Statistics and Computing*, pages 1–22, 2019.
- [11] Roberto Camassa and Darryl D. Holm. An integrable shallow water equation with peaked solitons. *Physical Review Letters*, 71(11):1661–1664, September 1993. doi: 10.1103/PhysRevLett.71.1661.
- [12] Bernard Delyon and Ying Hu. Simulation of conditioned diffusion and application to parameter estimation. *Stochastic Processes and their Applications*, 116(11):1660 – 1675, 2006. ISSN 0304-4149. doi: DOI:10.1016/j.spa.2006.04.004. URL <http://www.sciencedirect.com/science/article/B6V1B-4JVSSMK-1/2/cd3399cd4b5986a6c1757efd12c5b659>.
- [13] Mark Girolami and Ben Calderhead. Riemann manifold Langevin and Hamiltonian Monte Carlo methods. *Journal of the Royal Statistical Society: Series B (Statistical Methodology)*, 73(2):123–214, 2011. doi: 10.1111/j.1467-9868.2010.00765.x. URL <https://rss.onlinelibrary.wiley.com/doi/abs/10.1111/j.1467-9868.2010.00765.x>.
- [14] Ernst Hairer, Christian Lubich, and Gerhard Wanner. *Geometric numerical integration: structure-preserving algorithms for ordinary differential equations*, volume 31. Springer Science & Business Media, 2006.

- [15] Darryl D. Holm. Variational principles for stochastic fluid dynamics. *Proc. Mathematical, Physical, and Engineering Sciences / The Royal Society*, 471(2176), April 2015. ISSN 1364-5021. doi: 10.1098/rspa.2014.0963.
- [16] Darryl D Holm and Jerrold E Marsden. Momentum maps and measure-valued solutions (peakons, filaments, and sheets) for the epdiff equation. In *The breadth of symplectic and Poisson geometry*, pages 203–235. Springer, 2005.
- [17] Darryl D Holm and Tomasz M Tyranowski. Stochastic discrete hamiltonian variational integrators. *BIT Numerical Mathematics*, 58(4):1009–1048, 2018.
- [18] Darryl D. Holm, Jerrold E. Marsden, and Tudor S. Ratiu. The Euler-Poincaré Equations and Semidirect Products with Applications to Continuum Theories. *Advances in Mathematics*, 137(1):1–81, July 1998. ISSN 0001-8708. doi: 10.1006/aima.1998.1721.
- [19] Darryl D. Holm, J. Tilak Ratnanather, Alain Trouvé, and Laurent Younes. Soliton Dynamics in Computational Anatomy. *nlin/0411014*, November 2004. doi: 10.1016/j.neuroimage.2004.07.017. NeuroImage Vol 23, S170-178, 2004.
- [20] Th. Jeulin and M. Yor, editors. *Grossissements de filtrations: exemples et applications*, volume 1118 of *Lecture Notes in Mathematics*. Springer-Verlag, Berlin, 1985. ISBN 3-540-15210-5. doi: 10.1007/BFb0075765. URL <http://dx.doi.org/10.1007/BFb0075765>. Papers from the seminar on stochastic calculus held at the Université de Paris VI, Paris, 1982/1983.
- [21] SC Joshi and MI Miller. Landmark matching via large deformation diffeomorphisms. *Image Processing, IEEE Transactions on*, 9(8):1357–1370, 2000.
- [22] David G. Kendall. Shape Manifolds, Procrustean Metrics, and Complex Projective Spaces. *Bull. London Math. Soc.*, 16(2):81–121, March 1984. doi: 10.1112/blms/16.2.81.
- [23] Line Kühnel and Stefan Sommer. Computational anatomy in theano. In *Graphs in Biomedical Image Analysis, Computational Anatomy and Imaging Genetics*, pages 164–176. Springer, 2017.
- [24] Line Kühnel, Stefan Sommer, and Alexis Arnaudon. Differential geometry and stochastic dynamics with deep learning numerics. *Applied Mathematics and Computation*, 356:411–437, 2019.
- [25] Jean-Louis Marchand. Conditioning diffusions with respect to partial observations. *arXiv:1105.1608 [math]*, May 2011.
- [26] Bo Markussen. Large deformation diffeomorphisms with application to optic flow. *Comput. Vis. Image Underst.*, 106(1):97–105, April 2007. ISSN 1077-3142. doi: 10.1016/j.cviu.2005.09.006.
- [27] Stephen Marsland and Tony Shardlow. Langevin equations for landmark image registration with uncertainty. *SIAM J. Imaging Sciences*, 10:782–807, 2017.
- [28] Marcin Mider, Frank van der Meulen, and Moritz Schauer. Continuous-discrete smoothing of diffusions, 2020.
- [29] G. N. Milstein, Yu. M. Repin, and M. V. Tretyakov. Numerical methods for stochastic systems preserving symplectic structure. *SIAM Journal on Numerical Analysis*, 40(4):1583–1604, 2002. doi: 10.1137/S0036142901395588. URL <https://doi.org/10.1137/S0036142901395588>.
- [30] Xinyan Niu, Jianbo Cui, Jialin Hong, and Zhihui Liu. Explicit pseudo-symplectic methods for stochastic hamiltonian systems. *BIT Numerical Mathematics*, 58(1):

- 163–178, Mar 2018. ISSN 1572-9125. doi: 10.1007/s10543-017-0668-7. URL <https://doi.org/10.1007/s10543-017-0668-7>.
- [31] O. Papaspiliopoulos and G. Roberts. Importance sampling techniques for estimation of diffusion models. In *Statistical Methods for Stochastic Differential Equations*, Monographs on Statistics and Applied Probability, page 311337. Chapman and Hall, 2012.
- [32] J. Revels, M. Lubin, and T. Papamarkou. Forward-mode automatic differentiation in Julia. *arXiv:1607.07892 [cs.MS]*, 2016. URL <https://arxiv.org/abs/1607.07892>.
- [33] G. O. Roberts and O. Stramer. On inference for partially observed nonlinear diffusion models using the Metropolis-Hastings algorithm. *Biometrika*, 88(3):603–621, 2001. ISSN 0006-3444. doi: 10.1093/biomet/88.3.603. URL <http://dx.doi.org/10.1093/biomet/88.3.603>.
- [34] Gareth O. Roberts and Jeffrey S Rosenthal. Examples of adaptive MCMC. *Journal of Computational and Graphical Statistics*, 18(2):349–367, 2009.
- [35] L. C. G. Rogers and David Williams. *Diffusions, Markov processes, and martingales. Vol. 2*. Cambridge Mathematical Library. Cambridge University Press, Cambridge, 2000. ISBN 0-521-77593-0. Itô calculus, Reprint of the second (1994) edition.
- [36] Moritz Schauer, Frank van der Meulen, and Harry van Zanten. Guided proposals for simulating multi-dimensional diffusion bridges. *Bernoulli*, 23(4A):2917–2950, November 2017. ISSN 1350-7265. doi: 10.3150/16-BEJ833.
- [37] Stefan Sommer, Alexis Arnaudon, Line Kuhnel, and Sarang Joshi. Bridge Simulation and Metric Estimation on Landmark Manifolds. In *Graphs in Biomedical Image Analysis, Computational Anatomy and Imaging Genetics*, Lecture Notes in Computer Science, pages 79–91. Springer, September 2017. ISBN 978-3-319-67674-6 978-3-319-67675-3. doi: 10.1007/978-3-319-67675-3.8.
- [38] Mikkel Bille Stegmann, Rune Fisker, and Bjarne Kjær Ersbøll. Extending and applying active appearance models for automated, high precision segmentation in different image modalities. *Scandinavian Conference on Image Analysis*, pages 90–97, 2001.
- [39] Alain Trounev and François-Xavier Vialard. Shape splines and stochastic shape evolutions: A second order point of view. *Quarterly of Applied Mathematics*, 70(2):219–251, 2012. ISSN 0033-569X, 1552-4485. doi: 10.1090/S0033-569X-2012-01250-4.
- [40] Frank van der Meulen and Moritz Schauer. Bayesian estimation of discretely observed multi-dimensional diffusion processes using guided proposals. *Electron. J. Stat.*, 11(1):2358–2396, 2017. ISSN 1935-7524. doi: 10.1214/17-EJS1290. URL <http://dx.doi.org/10.1214/17-EJS1290>.
- [41] Frank van der Meulen and Moritz Schauer. BridgeLandmarks 0.3, January 2020. URL <https://github.com/mschauer/BridgeLandmarks.jl>. doi:10.5281/zenodo.3634591, <https://github.com/mschauer/BridgeLandmarks.jl>.
- [42] François-Xavier Vialard. Extension to infinite dimensions of a stochastic second-order model associated with shape splines. *Stochastic Processes and their Applications*, 123(6):2110–2157, June 2013. ISSN 0304-4149. doi: 10.1016/j.spa.2013.01.012.

- [43] Laurent Younes. *Shapes and Diffeomorphisms*. Springer, 2010. ISBN 978-3-642-12054-1.
- [44] Laurent Younes, Felipe Arrate, and Michael I. Miller. Evolutions equations in computational anatomy. *NeuroImage*, 45(1, Supplement 1):S40–S50, March 2009. ISSN 1053-8119. doi: 10.1016/j.neuroimage.2008.10.050.

APPENDIX A. PROOF OF PROPOSITION 1 ON STRATONOVICH TO ITÔ CORRECTION FOR AHS-MODEL

In coordinates, the stochastic equations for the AHS-model are

$$\begin{aligned} dq_i^\alpha &= \frac{\partial h}{\partial p_i^\alpha} dt + \sum_{l=1}^J \sigma_l^\alpha(q_i) \circ dW_t^l, \\ dp_i^\alpha &= -\frac{\partial h}{\partial q_i^\alpha} dt - \sum_{l=1}^J \sum_{\beta} \frac{\partial \sigma_l^\beta(q_i)}{\partial q_i^\alpha} p_i^\beta \circ dW_t^l, \end{aligned} \quad (33)$$

The same process with Itô's integrals, has the additional term

$$dq_i^\alpha + = \frac{1}{2} \frac{\partial \sigma_l^\alpha(q_i)}{\partial q_i^\beta} \sigma_l^\beta(q_i), \quad (34)$$

in the  $q$  equation and for the  $p$  equation

$$dp_i^\alpha + = \frac{1}{2} p_i^\gamma \frac{\partial \sigma_l^\gamma(q_i)}{\partial q_i^\beta} \frac{\partial \sigma_l^\beta(q_i)}{\partial q_i^\alpha} - \frac{1}{2} p_i^\beta \frac{\partial^2 \sigma_l^\beta(q_i)}{\partial q_i^\alpha \partial q_i^\gamma} \sigma_l^\gamma(q_i). \quad (35)$$

The extra term for  $q^\alpha$  given in (34) equals

$$\begin{aligned} \frac{1}{2} \sum_{\ell} \sum_{\beta} \frac{\partial \sigma_{\ell}^{\alpha}(q)}{\partial q^{\beta}} \sigma_{\ell}^{\beta}(q) &= \frac{1}{2} \sum_{\ell} \sum_{\beta} \gamma_{\alpha} \nabla_{\beta} \bar{k}_{\tau}(q - \delta) \gamma_{\beta} \bar{k}_{\tau}(q - \delta) \\ &= \frac{1}{2} \sum_{\ell} \langle \nabla \bar{k}_{\tau}(q - \delta), \gamma \rangle \bar{k}_{\tau}(q - \delta) \gamma_{\alpha}, \end{aligned}$$

which gives (31). Notice that we write  $\nabla_{\beta}$  to denote  $(\partial)/(\partial q^{\beta})$ .

For  $p^{\alpha}$  the first term on the right-hand-side of equation (35) is given by

$$\begin{aligned} \frac{1}{2} \sum_{\ell} \sum_u \sum_{\beta} p^u \frac{\partial \sigma_{\ell}^u(q)}{\partial q^{\beta}} \frac{\partial \sigma_{\ell}^{\beta}(q)}{\partial q^{\alpha}} &= \frac{1}{2} \sum_{\ell} \sum_u \sum_{\beta} \gamma_u \gamma_{\beta} \nabla_{\beta} \bar{k}_{\tau}(q - \delta) \nabla_{\alpha} \bar{k}_{\tau}(q - \delta) p^u \\ &= \frac{1}{2} \sum_{\ell} \nabla_{\alpha} \bar{k}_{\tau}(q - \delta) \langle \gamma, p \rangle \langle \gamma, \nabla \bar{k}_{\tau}(q - \delta) \rangle. \end{aligned}$$

This gives the first term in (32). The second term on the right-hand-side of equation (35) is given by

$$\begin{aligned} -\frac{1}{2} \sum_{\ell} \sum_u \sum_{\beta} p^{\beta} \frac{\partial^2 \sigma_{\ell}^{\beta}(q)}{\partial q^{\alpha} \partial q^u} \sigma_{\ell}^u(q) &= -\frac{1}{2} \sum_{\ell} \sum_u \sum_{\beta} p^{\beta} \gamma_{\beta} [\nabla_{\alpha} (\nabla_u \bar{k}_{\tau}(q - \delta))] \gamma_u \bar{k}_{\tau}(q - \delta) \\ &= -\frac{1}{2} \sum_{\ell} \langle (p, \gamma) \rangle \bar{k}_{\tau}(q - \delta) \nabla_{\alpha} (\langle \nabla \bar{k}_{\tau}(q - \delta), \gamma \rangle). \end{aligned}$$

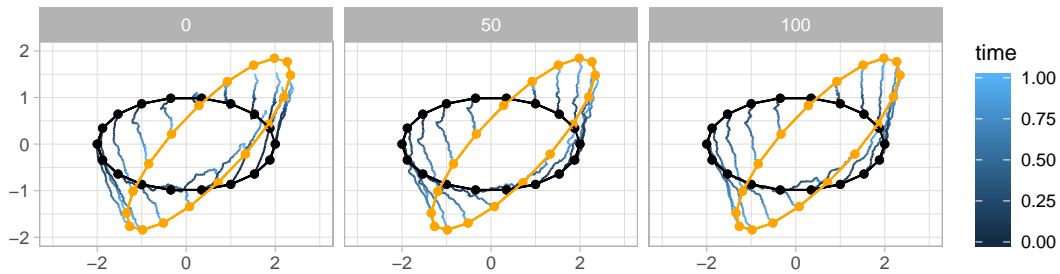


FIGURE 15. *Example 2, AHS-model.* Initial shape (black) and final shape (orange) using 18 landmarks. The curves connecting corresponding black/orange landmarks are simulated bridges. The different panels correspond to three different iteration numbers. The colouring of the paths captures evolution of the trajectories over time. Note that the initial paths (leftmost panel) does not fully connect the landmarks in the top-right corner.

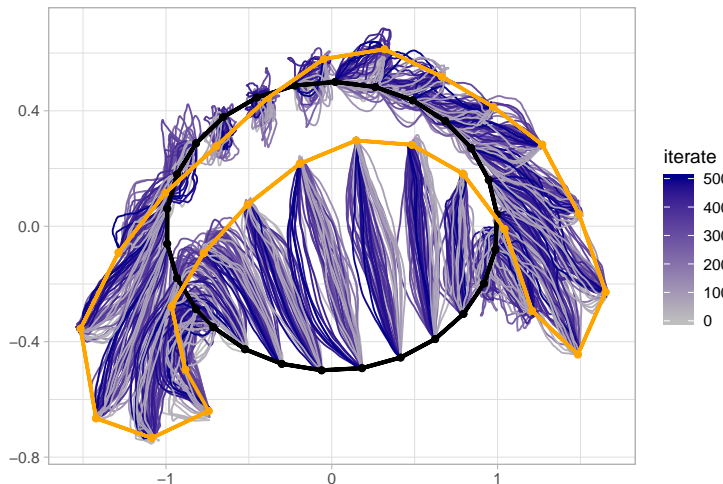


FIGURE 16. *Example 2, AHS-model.* Initial shape (black) and final shape (orange) using 18 landmarks. Each 10-th curve is plotted over 500 iterations. The grey dots indicate the centers of noise sources (denoted by  $\delta_j$  in the main text); the radii correspond to the value of  $\tau$  in the kernel  $\bar{k}_\tau$  (which was taken equal to 0.75).

This gives the second term in (32).

## APPENDIX B. MORE SIMULATION RESULTS

### B.1. Figures for Example 2 using the AHS-model. Figures 15, 16, 17 and 18.

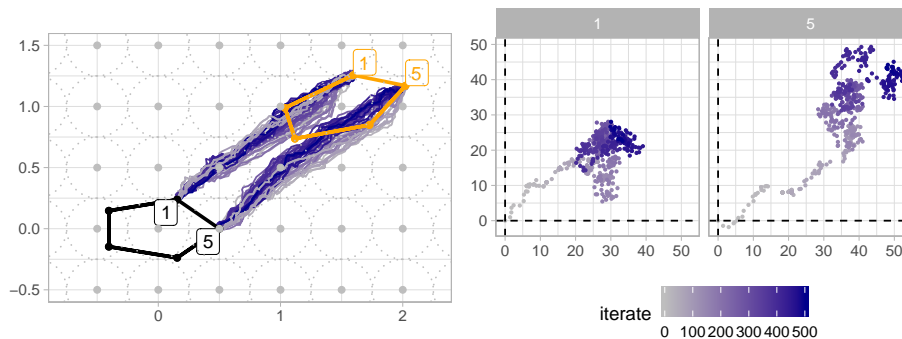


FIGURE 17. *Example 2, AHS-model.* Left: as in Figure 16, but only showing paths for 18 chosen landmarks. Right: for each of these landmarks the iterates for the initial momentum vector is shown (each dot corresponding to one iteration).

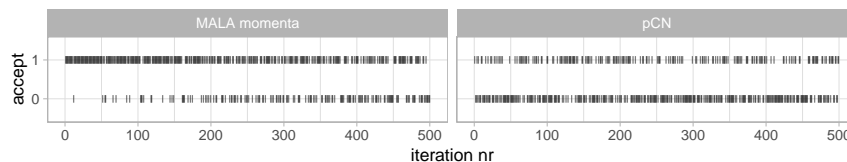


FIGURE 18. *Example 2, AHS-model.* Iterates showing acceptance/rejection of updating the initial momenta (left panel) and Wiener increments (right panel). 1 corresponds to acceptance; 0 to rejection.

AA: DEPARTMENT OF MATHEMATICS, IMPERIAL COLLEGE, LONDON SW7 2AZ, UK<sup>1</sup>

MS: MATHEMATICAL SCIENCES, CHALMERS UNIVERSITY OF TECHNOLOGY — UNIVERSITY OF GOTHENBURG

FM: DELFT INSTITUTE OF APPLIED MATHEMATICS (DIAM), DELFT UNIVERSITY OF TECHNOLOGY, THE NETHERLANDS

SS: DEPARTMENT OF COMPUTER SCIENCE (DIKU), UNIVERSITY OF COPENHAGEN, DK-2100 COPENHAGEN E, DENMARK

<sup>1</sup>*Current address:* Blue Brain Project, École polytechnique fédérale de Lausanne (EPFL), Campus Biotech, 1202 Geneva, Switzerland